Wind ~~Transport~~ Redistribution of Snow Impacts the Ka- and Ku-band Radar Signatures on Arctic Sea Ice

Vishnu Nandan[1,2*], Rosemary Willatt[3], Robbie Mallett[1,3], Julienne Stroeve[1,3], Torsten Geldsetzer[2], Randall Scharien[4], Rasmus Tonboe[5], John Yackel[2], Jack Landy[6], David Clemens-Sewall[7], Arttu Jutila[8], David N. Wagner[9,10], Daniela Krampe[8], Marcus Huntemann[11], Mallik Mahmud[2], David Jensen[1], Thomas Newman[3], Stefan Hendricks[8], Gunnar Spreen[11], Amy Macfarlane[9], Martin Schneebeli[9], James Mead[12], Robert Ricker[13], Michael Gallagher[14], Claude Duguay[15,16], Ian Raphael[7], Chris Polashenski[7], Michel Tsamados[3], Ilkka Matero[8] and Mario Hoppmann[8].

[1]Centre for Earth Observation Science (CEOS), University of Manitoba, Canada
[2]Department of Geography, University of Calgary, Canada
[3]Centre for Polar Observation and Modeling, Earth Sciences, University College London, UK
[4]Department of Geography, University of Victoria, Canada
[5]DTU Space, Technical University of Denmark, Denmark
[6]Centre for Integrated Remote Sensing and Forecasting for Arctic Operations (CIRFA), UiT The Arctic University of Norway, Tromsø, Norway
[7]Thayer School of Engineering, Dartmouth College, USA
[8]Alfred Wegener Institute, Helmholtz Centre for Polar and Marine Research, Bremerhaven, Germany
[9]WSL Institute for Snow and Avalanche Research (SLF), Davos, Switzerland
[10]CRYOS, School of Architecture, Civil and Environmental Engineering, EPFL, Lausanne, Switzerland
[11]Institute of Environmental Physics, University of Bremen, Germany
[12]ProSensing Inc, Amherst, MA, USA
[13]Norce Norwegian Research Centre AS, Bergen, Norway
[14]Physical Sciences Laboratory, NOAA, USA
[15]Department of Geography and Environmental Management, University of Waterloo, Canada
[16]H2O Geomatics Inc., Waterloo, Canada

Correspondence: Vishnu Nandan (Vishnu.Nandan@umanitoba.ca)

Abstract: Wind-driven redistribution of snow on sea ice~~ transport~~ alters its topography and microstructure, yet ~~through snow redistribution controlled by deposition and erosion.~~ t~~T~~he impact of these processes on radar signatures is poorly understood. Here, we examine the effects of snow redistribution over~~n~~ Arctic sea ice on~~from~~ radar waveforms and backscatter signatures obtained from a surface-based, fully-polarimetric Ka- and Ku-band radar~~, waveforms and backscatter signatures, acquired using a surface-based, fully-polarimetric Ka- and Ku-band radar~~ at incidence angles between 0° (nadir) and 50°. Two ~~Measurements were obtained during two~~ wind events in November 2019 during the MOSAiC International Arctic Drift E~~e~~xpedition are evaluated. During both events, changes in Ka- and Ku-band radar waveforms and backscatter coefficients at nadir are observed, coincident with surface topography changes measured by a terrestrial laser scanner~~ are observed~~. At both frequencies, redistribution caused snow densification at the surface and the uppermost layers, increasing~~events increased~~ the scattering at the air/snow interface at nadir ~~viewing angles~~ and its prevalence as the dominant radar scattering surface. ~~, due to wind-induced snow densification at the snow surface densifying the snow surface and uppermost layers. At both frequencies, snow redistribution events increased the dominance of the air/snow interface at nadir as the dominant radar scattering surface, due to wind densifying the snow surface and uppermost layers.~~ The~~ radar~~ waveform data also detected the presence of previous air/snow interfaces, buried beneath newly deposited snow. The additional scattering from previous air/snow interfaces could therefore affect the range retrieved from Ka- and Ku-band satellite ~~radar~~ altimeters. With increasing incidence angles, ~~T~~the relative scattering contribution of the air/snow interface decreases, and the snow/sea ice interface scattering increases~~ with increasing incidence angles~~. Relative to pre-wind event conditions, azimuthally averaged backscatter at nadir during the wind events increases by up to 8 dB (Ka-band) and 5 dB (Ku-band). Results show~~Binned backscatter within 5° azimuth bins reveals~~ substantial backscatter variability within the ~~radar~~ scan area at all incidence angles and polarizations, in response to increasing wind speed and changes in wind direction. ~~The sensitivity of the co-polarized phase difference is linked to changes in snow settling and temperature-gradient induced grain metamorphism, demonstrating the potential of the radar to discriminate between newly deposited and older snow on sea ice.~~ Our results have~~document~~ the impact of wind ~~reveal the importance of wind, through its geophysical impact on Ka- and Ku-band radar signatures of snow covered sea ice~~, which ~~and has~~ implications for reliable interpretation of airborne and satellite radar measurements of snow-covered sea ice.

1 Introduction

Wind plays an important role in shaping the spatial distribution of snow depth and snow water equivalent (SWE) over sea ice (Moon et al., 2019; Iacozza & Barber, 2010). Wind alters snow temperature gradients through wind pumping (Colbeck, 1989), structural anisotropy (Leinss et al., 2020), and snow grain geometry (Löwe et al., 2007). Furthermore, wind affects the residence and sintering time of snow close to the surface, facilitating depositional snow dune growth and erosional processes (Trujillo et al., 2016). Fluctuating wind speed~~s~~ and direction~~s~~ ~~thus~~ modify snow surface topography and density via wind scouring and compaction of snow (Lacroix et al., 2009). Depending on the ice surface roughness (e.g., level ice, pressure ridges, hummocks etc.), wind will result in the formation of heterogeneities at different scales, from ~~heterogeneously distributed~~ ~~cm-scale~~ ripple marks to snow bedforms and drifts ~~on the scale of 10's of meters~~ (Filhol & Sturm, 2015; Sturm et al., 1998). This further alters the geometric, aerodynamic, and radar-scale roughness ~~on sea ice~~ (Savelyev et al., 2006; Fung & Eom, 1982).

~~Since wind redistribution of snow impacts snow depth distribution and SWE, this can in turn alter Ka- and Ku-band radar backscatter signatures used in the airborne- and satellite-based retrievals of~~ snow depth, ~~sea ice freeboard and thickness.~~ Under cold ~~and calm~~ snow conditions, a common assumption in radar altimetry is that the dominant scattering surfaces of co-polarized Ka- and Ku-band radar signals correspond to the air/snow and snow/sea ice interfaces, respectively (e.g. Armitage et al., 2015; Tilling et al., 2018). ~~, due to dominant surface scattering from these interfaces (Fung & Eom, 1982)~~. For synthetic aperture radar (SAR) and scatterometry, variations in snow grain microstructure ~~or from inclusions within the sea ice~~ influence the proportion of surface and volume scattering to the total radar backscatter (Nandan et al., 2017~~Fung, 1994~~). Winds can roughen/~~or~~smoothen the snow surface on relatively short time scales, altering~~modifying~~ the Ka- and Ku-band surface and/or volume scattering contributions to ~~the dominant scattering surfaces and~~ total radar backscatter.

Very little is known about how wind redistribution of snow impacts snow depth, SWE, and ice thickness retrievals from airborne and satellite radars (e.g., Yackel & Barber, 2007; Kwok & Cunningham, 2008; Kurtz et al., 2009; Kurtz & Farrell, 2011~~; Glissenaar et al., 2021~~). Due to repeat airborne and satellite ground-tracks often occurring weeks/months apart and sea ice drift, it is challenging to measure radar backscatter changes resulting from wind redistribution~~-~~, on the same area of ice over time. Nevertheless, Kurtz & Farrell (2011) assumed snow redistribution caused an anomalous snow depth decrease in 2009 over multi-year sea ice in the Canadian Archipelago (CA), retrieved from two Operation IceBridge (OIB) snow radar flights, acquired three weeks apart. Yackel & Barber (2007) speculated that snow redistribution on first-year sea ice in the CA was, in part, responsible for a ~~caused a~~ change in retrieved SWE of up to 7 cm, derived from two C-band RADARSAT-1 images~~, acquired~~ 45 days apart. ~~To represent small-scale spatial variability due to snow redistribution that are not captured in the large-scale satellite products, studies have developed snow redistribution functions, designed for high resolution laser altimetry data (e.g., Kwok & Cunningham, 2008; Kurtz et al., 2009). However, Glissenaar et al. (2021) applied the snow redistribution scheme developed by Kurtz et al. (2009) on the OIB-derived radar freeboard and snow depth products for the~~

~~Arctic Ocean and found no correlation between radar freeboard and snow depth estimates averaged over the footprint-scale of the CryoSat-2 (300 m) and ENVISAT (2 km) radar altimeters. They concluded that applying a snow redistribution scheme on radar altimetry freeboard data would not improve the sea ice freeboard-to-thickness conversion.~~

T~~Overall, t~~o better understand the impact of snow redistribution on Ka- and Ku-band radar signatures, we require unambiguous in-situ measurements of snow physical properties and meteorological observations during wind events, sampled coincidentally with ~~surface-based~~ radar measurements. This bridges a fundamental knowledge gap, and potentially allows improved modelling of Ka- and Ku-band radar waveforms and backscatter~~ at multiple polarizations and incidence angles~~. This in turn may improve interpretation of Ka- and Ku-band radar signatures from presently operational SARAL/AltiKa (Guerreiro et al., 2016), CryoSat-2 (Lawrence et al., 2018), Sentinel-3 (Lawrence et al., 2021), ScatSat-1 (Singh & Singh, 2020) and the upcoming Ka-/Ku-band CRISTAL altimetry (Kern et al., 2020) and SWOT satellite missions (Armitage & Kwok, 2021).

In this~~our~~ study, we investigate wind-induced changes to~~in~~ snow physical properties and topography on Ka- and Ku-band dominant scattering surfaces and backscatter using a surface-based, fully-polarimetric, Ku~~a~~- and Ka~~u~~-band radar (KuKa radar; see Stroeve et al., 2020) ~~that was~~ deployed during the 2019-20 Multidisciplinary drifting Observatory for the Study of Arctic Climate (MOSAiC) expedition (Krumpen et al., 2020). W~~Here, w~~e present ~~the analysis of~~ data from~~gathered between~~ 9 to~~and~~ 16 November 2019, assessing the effects of two separate Wind Events (~~'~~WE1~~'~~ and ~~'~~WE2~~'~~). First, we describe the KuKa radar system, the time series of meteorological observations, snow physical properties, and snow surface topography. Next, we investigate the impact of snow redistribution on KuKa~~Ka- and Ku-band~~ radar echograms and waveforms, examining changes in dominant scattering surfaces and~~,~~ radar backscatter~~ and co-polarized phase difference~~. Finally, we discuss the relevance of our findings to improving retrievals of snow/sea ice geophysical variables by airborne and satellite radars.

2. Data and Methods

2.1 Surface-Based Ka- and Ku-band Polarimetric Radar (KuKa Radar)

During the MOSAiC expedition, the ~~German~~ research icebreaker *R/V Polarstern* drifted with a sea ice floe across the central Arctic Ocean over a full annual cycle (~~See Figure 1 in~~ Nicolaus et al., 2022). The floe was dominated by second-year ice with~~including ~ 60%~~ refrozen melt ponds making up ~ 60% of the surface area (Krumpen et al., 2020). The Remote Sensing Site (RSS) was first established on the floe on 18 October 2019, where the KuKa radar was deployed on ~ 80 cm thick, laterally homogeneous~~homogenous~~, and undeformed sea ice.

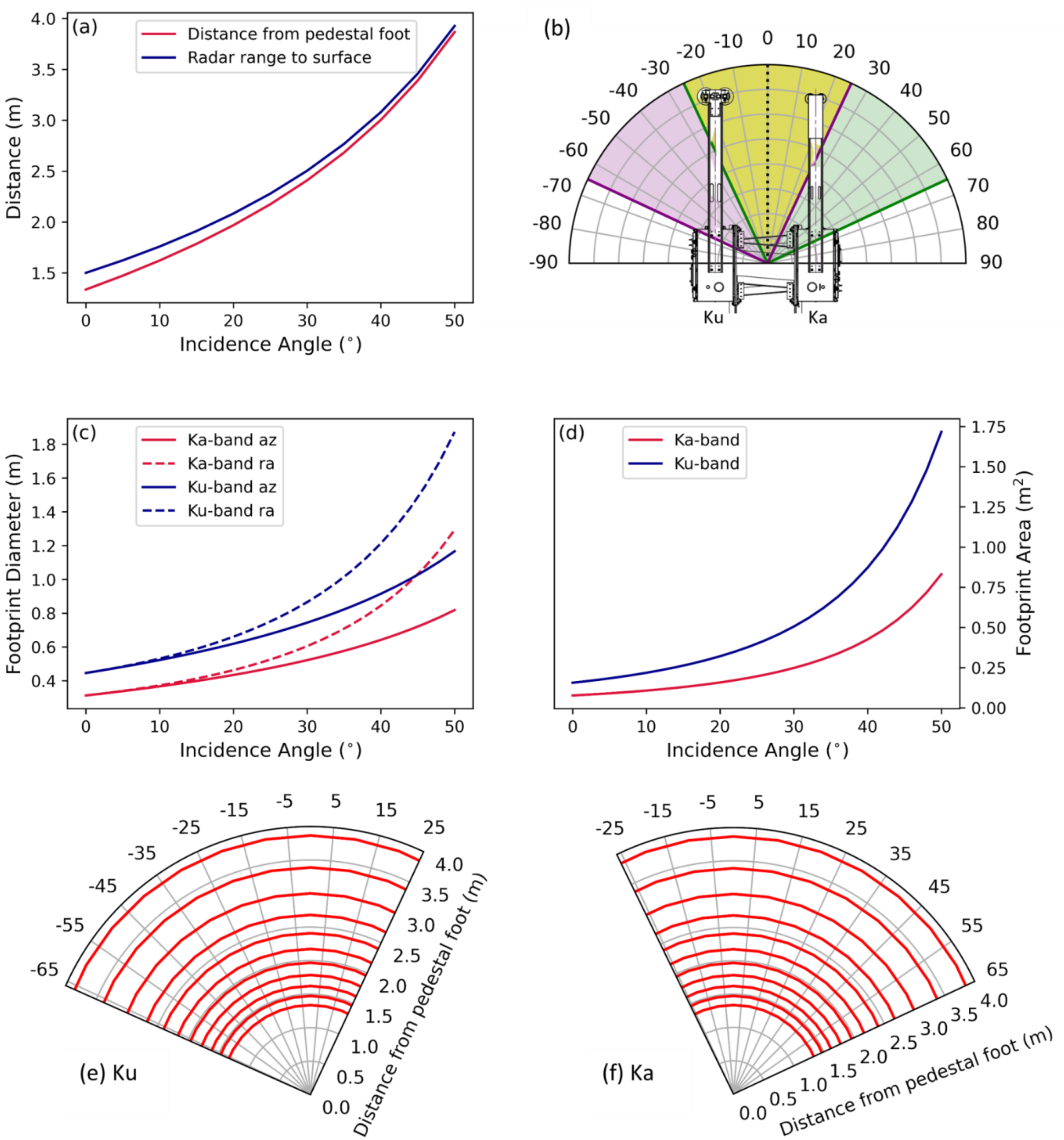

(a)
Distance from pedestal foot
Radar range to surface
Distance (m)
Incidence Angle (°)
(b)
Ku
Ka
(c)
Ka-band az
Ka-band ra
Ku-band az
Ku-band ra
Footprint Diameter (m)
Incidence Angle (°)
(d)
Ka-band
Ku-band
Footprint Area (m²)
Incidence Angle (°)
(e) Ku
Distance from pedestal foot (m)
(f) Ka
Distance from pedestal foot (m)

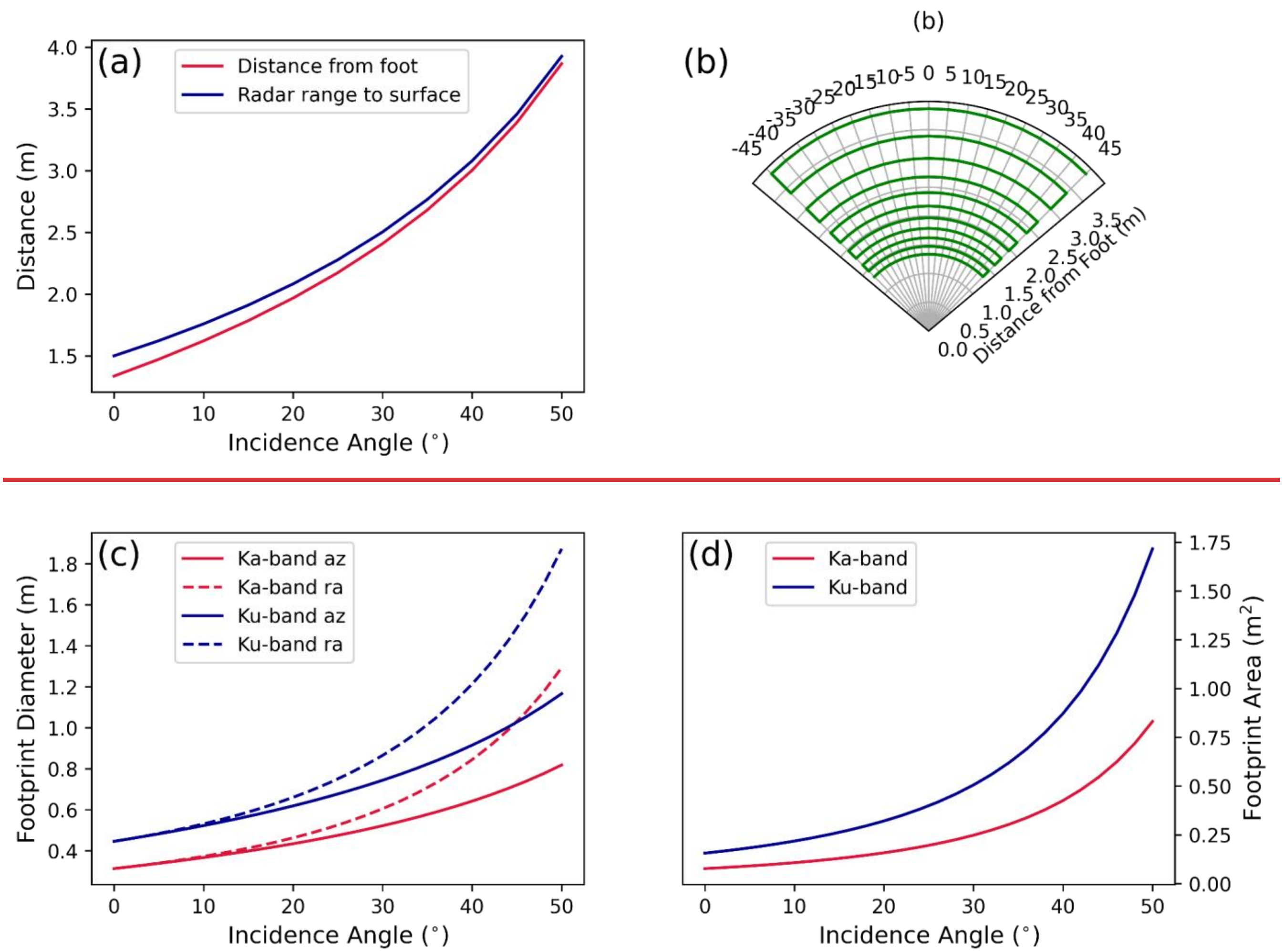

Figure 1: KuKa radar geometry illustrating (a) radial distance and radar range from the pedestal foot; (b) KuKa radar azimuth scan pattern projected based on the positioner axis coordinate system (b) scan pattern of radar projected onto a level surface; (c) diameter of radar scan area, measured radially ('ra') and azimuthally ('az'); ~~and~~ (d) area of radar scan area; (e) and (f) Ku- and Ka-band scan area of the KuKa radar, respectively. In panel (b), the region between purple and green lines are the respective Ku- and Ka-band scan area (separately illustrated~~shown~~ in panels (e) and (f), while the yellow region in (b) is the overlapping scan area~~.~~

The KuKa radar transmits at Ka- (30-40 GHz) and Ku-band (12-18 GHz) frequencies and measures the return radar power (in dBm) as a function of range (Stroeve et al. 2020). The radar acquires data across a fixed azimuth (θ_{az}) range, at discrete incidence angle (θ_{inc}) intervals. The radar operates in all vertical (V) and horizontal (H) linear polarization transmit and receive combinations: VV, HH, HV, and VH. ~~As such, it is fully-polarimetric, enabling derivation of many polarimetric parameters including the co-polarized phase difference (CPD), analysed here.~~

The central frequency of the radar chirps were set to be close to~~to match~~ the Ka-band of AltiKa (35 GHz) and the Ku-band of CryoSat-2 (13.575 GHz). The KuKa radar bandwidth is considerably higher than the bandwidth of AltiKa and CryoSat-2, allowing improved range resolution of 1.5 cm for Ka-band and 2.5 cm for Ku-band relative to 30 cm and 46 cm for AltiKa and CryoSat-2, respectively. The radial distance and range from the pedestal, the scan area diameter, and scan area from ~~nadir to~~ θ_{inc} = 0° - 50° are illustrated~~shown~~ in Figure 1. During MOSAiC, the KuKa radar scanned~~s~~ over a 90° continuous θ_{az} range width for every 5° interval in θ_{inc}. The KuKa radar takes ~ 16 seconds (i.e. 5.7° per second) over a 90° θ_{az} width to acquire data across an incidence angle scan line and ~ 2.5 minutes for one complete scan between θ_{inc} = 0° - 50°. However, there is a ~ 20° offset between the individual radar antennas and the radar positioner axis origin. Therefore, the Ku-band antenna scans between -65° to +25° θ_{az} range (region between purple lines) from -25° to +65° for Ka-band (region between green lines) (Figure 1(b), (e) and (f)). This also means that the Ku- and Ka-band scan area overlap for a given radar 'shot' is θ_{inc} dependent. The yellow region between green and purple lines in Figure 1b between -25° and +25° is the overlapping Ku- and Ka-band scan area. The antenna beamwidth (6 dB two-way) is 16.9° and 11~~6~~.9° for Ku~~a~~- and Ka~~u~~- bands, respectively. Therefore, the size of the radar scan area on the snow is dependent on frequency, height of the antenna above the snow surface, and θ_{inc}. Further description of the radar specifications, signal processing, polarimetric calibration routine, signal-to-noise and error estimation is documented in Stroeve et al. (2020).

At the RSS, the radar acquired scans every 30 mins over the 90° θ_{az} width and θ_{inc} discrete increments, ~~called a scan line, between~~ these ~~nadir (0°) and θ_{inc} = 50°, at 5°~~ discrete ~~increments~~. Between 9 and 15 November, a total of 325 scans were collected. T~~Following WE2, t~~he ice supporting the RSS broke up on 16 November, and the measurements were stopped until it was safe to redeploy the radar.

2.2 Meteorological and Snow Property Data

A 10-m tall meteorological station installed ~ 100 m away from the RSS monitored air temperature (°C), relative humidity (%), air pressure (hPa), wind speed (m/s) and wind direction (°), all at 2 m height~~s from the surface~~. Wind direction is denoted ~~denoted~~ with respect to geographic north (0°). Measurements were acquired ~~and logged~~ every second (Cox et al., 2021) and resampled to 30-minute averages, to match the radar scan intervals.

A thermal infrared (TIR) camera (Infratec VarioCam HDx head 625, assuming emissivity 0.97 at 7.5-14 µm wavelength; Spreen et al., 2022) measured snow surface temperature (°C), every 10 minutes. Two digital thermistor chains (DTC) installed close to the RSS measured near-surface, snow, and sea ice temperature evolution at 2 cm vertical intervals. No destructive snow sampling was done underneath the KuKa radar scan area. Instead, snow depth measurements were made~~sampled using a metre stick~~ close to the radar on 4 and 14 November. Profiles of the penetration resistance force of the snow were collected before, during and after WE1 and WE2 using a Snow Micro-penetrometer (SMP; Johnson & Schneebeli, 1999) at the ~~‘~~Snow1~~’~~, ~~‘~~Snow2~~’~~ and the RSS sites (see locations in Figure 4). Five SMP profiles per pit were recorded weekly. To compare initial density and SSA between the RSS and the Snow1 and Snow2 locations at the beginning of November, one SMP profile from the RSS was taken on 4 November. The force profiles were converted into density and specific surface area (SSA) following King et al. (2020) and Proksch et al. (2015) parameterizations, respectively, that also worked well ~~for snow~~ during the MOSAiC winter (Wagner et al., 2022).

2.3 Snow Surface Topography

An optical~~Footage from a visual surveillance closed-circuit television (CCTV)~~ camera was used to visualise snow surface topography changes within the radar scan area (Spreen et al., 2021). In addition, Terrestrial Laser Scanning (TLS) data of snow surface topography were collected on 1, 8 and 15 November using a Riegl VZ1000~~, which generated point clouds of the snow surface topography in the radar scan area~~. Scan positions were registered in RiSCAN (Riegl's data processing software) using reflectors permanently frozen to the ice and levelled based on the VZ1000's built-in inclination sensor. Wind-blown snow particles were removed from the data by FlakeOut filtering (Clemens-Sewall et al., 2022). Filtered data were aligned to one another by matching reflectors and other tie-points. To transform the TLS data into the KuKa radar's reference frame, the outlines of the radar’s pedestal column and the antenna arms were manually picked in the TLS data.

A non-linear least squares optimization method using SciPy (Virtannen et al 2020) was then implemented to estimate the best fitting circle and rectangle to match the pedestal column and the antenna arms, respectively. The centre of the pedestal was used as the horizontal origin, the centre of the antennas was used for orientation, and the antenna height at nadir position was used as the vertical origin. Within the radar’s reference frame, a polar grid was defined with radial increments of 0.25 m and azimuthal increments of 10°. The surface height in the radar reference frame (a.k.a. the vertical distance from the surface to the radar antennas at nadir) for each grid cell was calculated by averaging the vertical position of each TLS point within that grid cell.

2.5 Radar Waveforms and ~~,~~ Backscatter~~ and Co-polarized Phase Difference~~

~~Radar waveform analysis is performed to determine how WE1 and WE2 affected the surfaces and volumes detected by the radar, especially the dominant scattering surface.~~ Waveforms from each sampling time across ~~the~~ θ_{az} ~~range~~ were~~are~~ recorded and overlaid with the TLS data to identify~~aid in interpretation of~~ where ~~in the snow/sea ice~~ the Ka- and Ku-band backscatter originated from (Section 3.2). D~~For the waveform analysis, d~~econvolved waveforms were~~are~~ used (~~described in~~ Stroeve et al., 2020~~2~~),~~.~~ ~~To summarise, data are deconvolved~~ using waveforms from a refrozen lead located close to the RSS in January 2020 ~~(see Stroeve et al, 2020),~~ to ~~which~~ provide~~ed~~ a specular return useful for reducing the appearance of sidelobes that result from non-ideal behaviour of the RF electronics, as well as internal reflections in the radar. Waveform echograms were~~are~~ used to illustrate how the return waveforms from within the overlapping scan area changed between~~over~~ WE1 and WE2. The normalized radar cross section per unit area (NRCS) was~~is~~ calculated based on the range-power profiles following the standard beam-limited radar range equation (Ulaby et al., 2014), given by:

$$NRCS = \frac{8ln\,(2)h^2\sigma_c}{\pi R_C^4 \theta_{3dB}^2 cos\,\theta}\left(\frac{\widetilde{P_r}}{\widetilde{P_{rc}}}\right)$$

where h is the antenna height, R_C is the range to the corner reflector, θ_{3dB} is the one-way half-power beamwidth of the antenna and $\widetilde{P_r}$ and $\widetilde{P_{rc}}$ are the received power from the snow and the corner reflector, respectively.

The peak power in the radar waveforms used for calculating NRCS is determined by locating the highest peak in the waveform averaged across all polarisations. For waveform analysis, we calculated the NRCS values at nadir for the air/snow and snow/ice interfaces by integrating the power over the waveform peaks within +/- 2 dB either side from the overlapping scan area ~~depicted in Figure 1(b)~~ (Section 3.2). Next, we calculated the NRCS value integrated over the entire snow volume based on the power contained within this peak over an incidence angle scan line, by integrating over the range bins where the power falls below a threshold, ~~are~~ set to -50 dB on either side of the peak for Ka-band data, and -20 dB (-40 dB) on the on the smaller-range (larger-range) sides for Ku-band data. The NRCS was averaged across the overlapping scan area across the entire 90° θ_{az} range, at discrete θ_{inc} = 0°, 15°, 35° and 50°, to demonstrate scan area-scale variability in backscatter during the two wind events (section 3.3). ~~This NRCS calculation is derived from the The return power is integrated over the entire snow volume, so the NRCS values include scattering contributions at the air/snow and snow/ice interfaces as well as from within the snow volume. First, we calculate the NRCS values for the air/snow and snow/ice interfaces by integrating the power over the waveform peaks within +/- 2 dB either side from the overlapping footprint area depicted in Figure 1(b) (Section 3.2). Next, we calculate the NRCS averaged across the overlapping footprint areaentire 90° θ_{az} range, at discrete θ_{inc} = 0°, 15°, 35° and 50°, to demonstrate footprint-scale variability in backscatter during the two wind events (section 3.3).~~

To investigate the sub-scan area scale backscatter variability caused by surface heterogeneity, as well as the range to the dominant scattering surface that could have changed ~~before,~~ during sampling~~and after WE1 and WE2~~, we used azimuth 'sectoring' and analysed the NRCS averaged at 5° wide θ_{az} bins ~~(i.e., negative θ_{az} sectors between -45° to -40°… -5° to 0° and positive θ_{az} sectors between 0° to +5°… +40° to +45°)~~ (Figure 1(e) and (f)~~b~~). Azimuth 'sectoring' has an impact on the number of independent samples in range along a 5° θ_{az} bin, since a smaller area is used for averaging (Table 1). The number of independent samples is estimated based on the following steps: a) determine the distance between the 6 dB points below the radar range peak on either side of the peak, b) divide the 6 dB range by the range resolution. This is a measure of the number of independent samples in range, c) divide the azimuth width (90° and 5° in our study) by the azimuth beamwidth and multiply by 2, and d) the total number of independent samples would then be the number of independent samples in range multiplied by the number of independent samples in azimuth (Doviak & Zrnić, 1984). ~~by dividing half the antenna beamwidth by the θ_{az} angular width (90° and 5° in this study)width, then multiplied by the number of range gates (Geldsetzer et al., 2007).~~

Table 1: Number of independent samples at Ka- and Ku-band frequencies at nadir and θ_{inc} = 50° at θ_{az} = 90° and along a 5° bin

Frequency	Nadir		θ_{inc} = 50°	
	θ_{az} = 90°	θ_{az} = 5°	θ_{az} = 90°	θ_{az} = 5°
Ka-band	487	48	1609	439
Ku-band	198	34	1252	376

Within every θ_{inc} scan, VV, HH and HV are derived from the complex covariance matrix ~~(second-order derivative of the scattering matrix containing amplitude and phase)~~, while VH is discarded based on ~~the observed~~ reciprocity of cross-polarized channels (i.e., HV ~ VH) (Ulaby et al., 2014). ~~We also use the derived co-polarized phase difference (CPD) given by arctan~~ $\left[\frac{Im\langle S_{HH}S_{VV}^*\rangle}{Re\langle S_{HH}S_{VV}^*\rangle}\right]$ ~~uniformly distributed over [-π, π] (Ulaby et al., 2014). CPD is sensitive to the snow structural anisotropy changes (e.g. Leinss et al., 2016) resulting from snow residence and settling time, as well as snow metamorphic change resulting from the snow temperature gradient (Löwe et al., 2011; Leinss et al., 2020). Studies on terrestrial snow from X-band SAR show that new snow has a horizontal alignment of snow crystals that results in greater anisotropy and CPD (i.e., positive phase shift) (Voglimacci-Stephanopoli et al., 2022; Leinss et al., 2016). With subsequent temperature-gradient induced metamorphism, the growth of vertical structures overpowers the build-up of horizontal structures during snow settling, decreasing the anisotropy and CPD (i.e., negative phase shift) (Leinss et al., 2016).~~ In Section 3.3.2, we show the changes in backscatter signature variability~~signatures and CPD variability~~ across the KuKa radar scan area at 5° wide θ_{az} bins at specific times~~stamps~~ on 9, 11 and 15 November.

3. Results

3.1 Meteorological and Snow Conditions

3.1.1 WE1 and WE2

~~The floe experienced two wind events between 11 and 16 November 2019.~~ WE1 started ~ 0745 UTC ~~occurred~~ on 11 November and lasted until ~ 0800 UTC on 12 November when winds ~12 m/s originated ~~blew~~ from the SW to SE ~~directions~~ (Figure 2 and 3c). WE2 started ~ 0900 UTC on 15 November, when a low-pressure system began to intensify (Figure 3b~~a~~). The wind direction shifted from SW to W, and speeds increased to ~ 15 m/s and continued until ~ 1900 UTC on 16 November (Figure 2 and 3c). During WE2, the strong low-pressure system dropped ~~just~~ below 995 hPa (Figure 3d~~a~~) and the air temperature~~s~~

reached ~~as high as~~ -5.5°C (Figure 3a). The warm air advection was accompanied by a steep increase in relative humidity to~~that reached~~ > 90% (Figure 3d~~b~~).

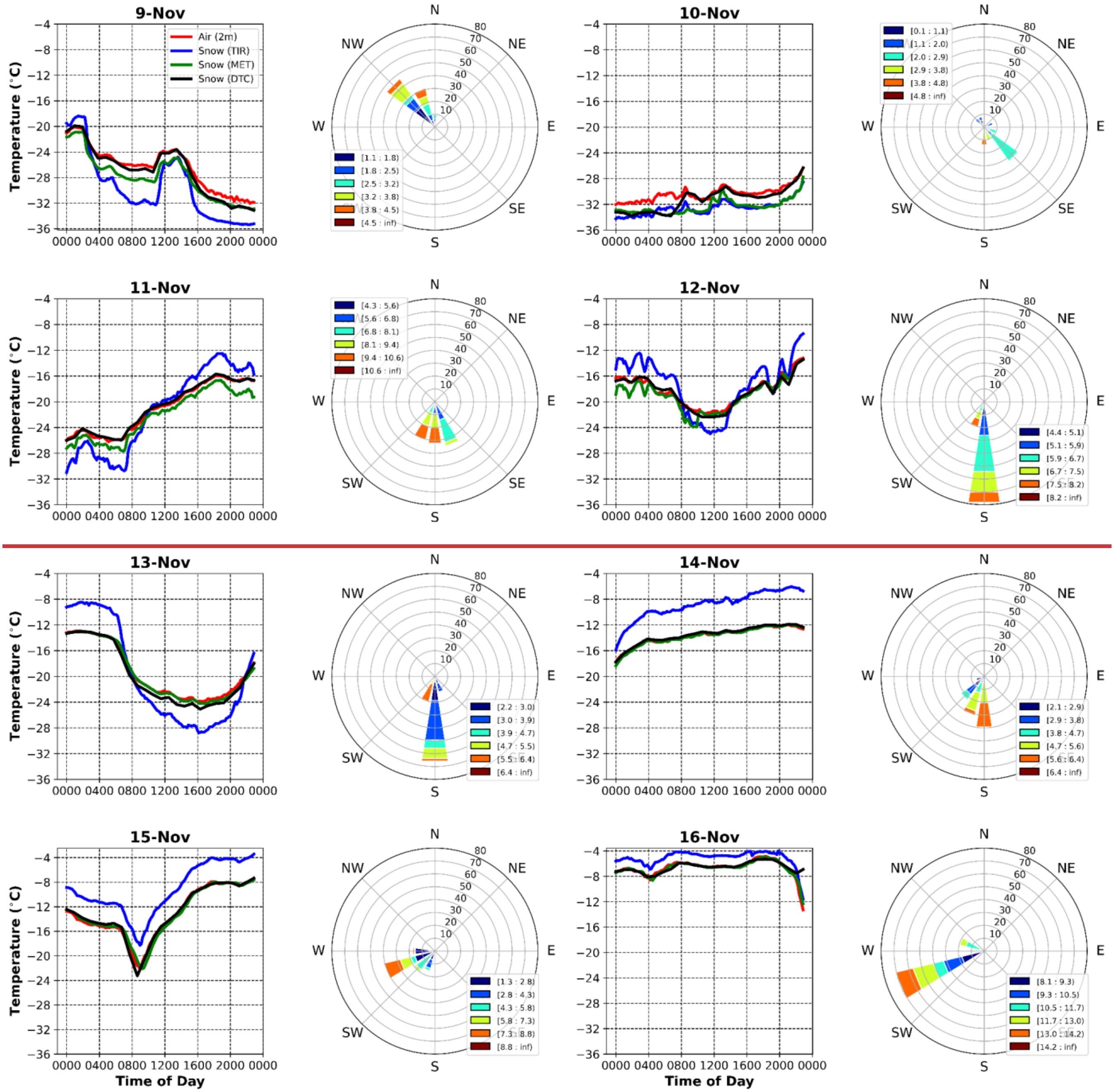

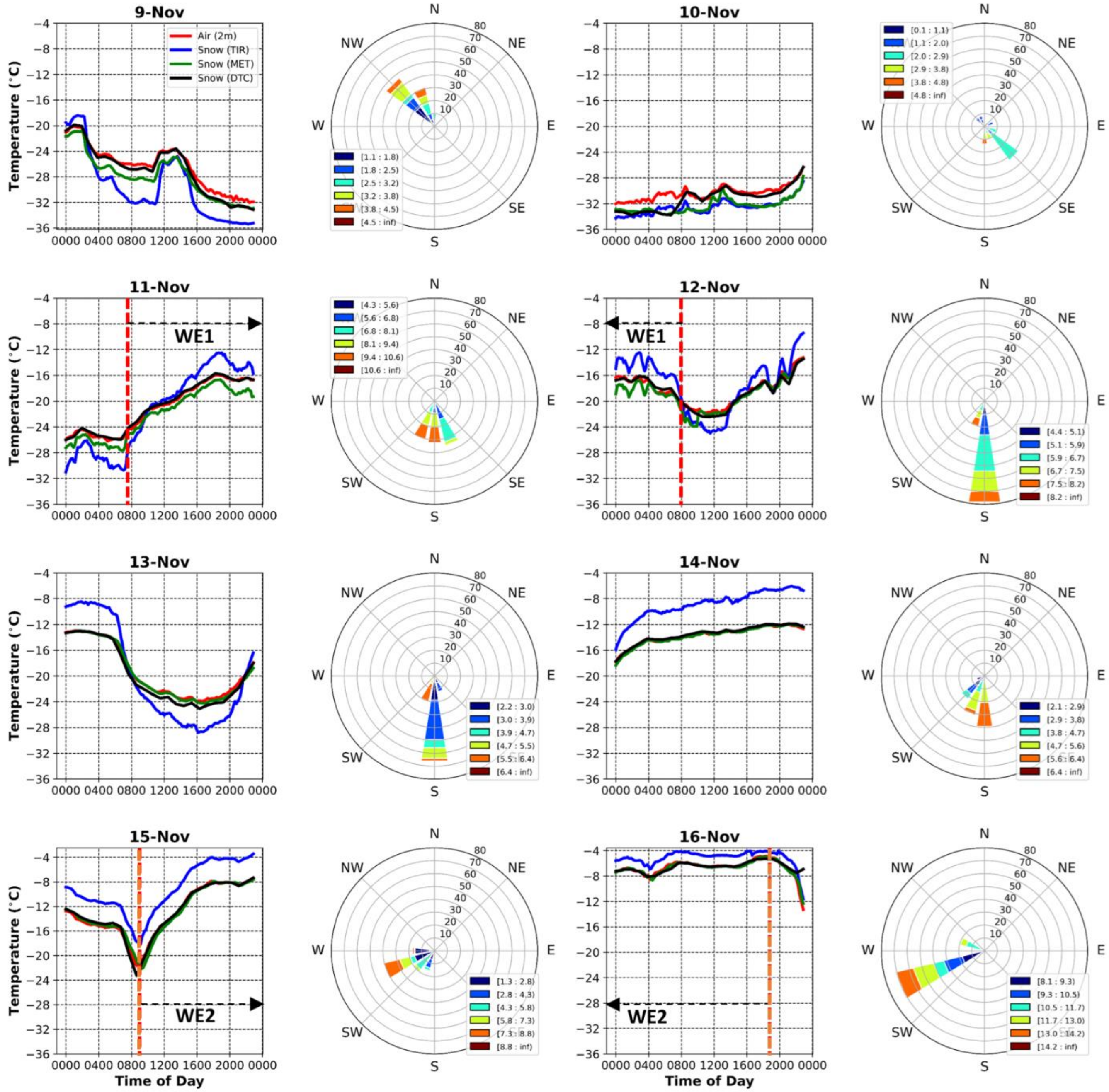

Figure 2: Line plots illustrate daily, 30-min averages of 2 m air temperature (MET tower) and snow surface temperature measurements from the TIR camera, MET tower and DTC sensors; acquired between 9 and 16 November. Wind rose plots illustrate corresponding wind

speed (m/s) and direction (°) measurements recorded by the MET tower. All times are UTC. Dotted red and orange lines indicate the onset of WE1 and WE2, respectively, supported by black arrows.

3.1.2 Snow Temperature, Density and Microstructure

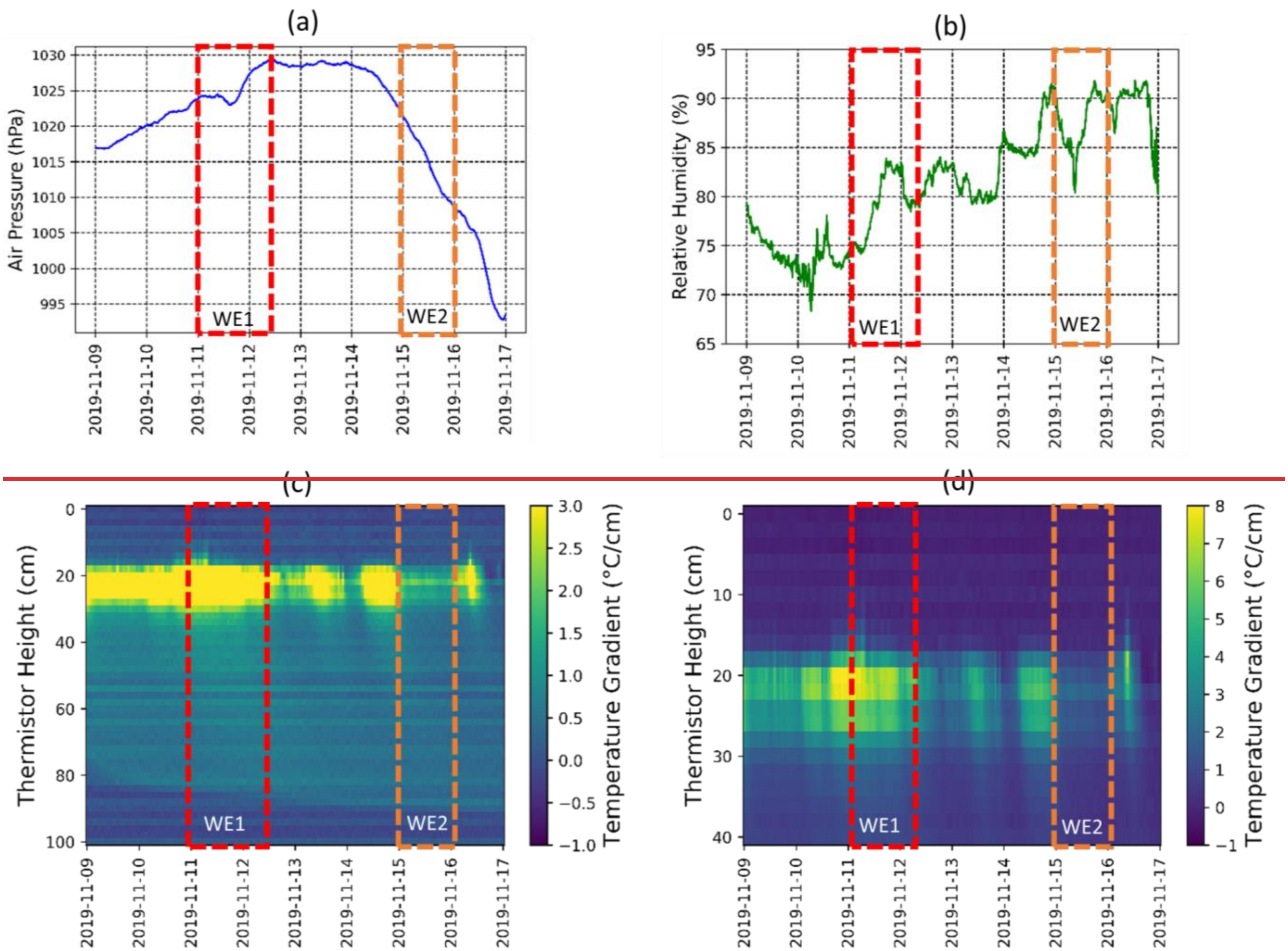

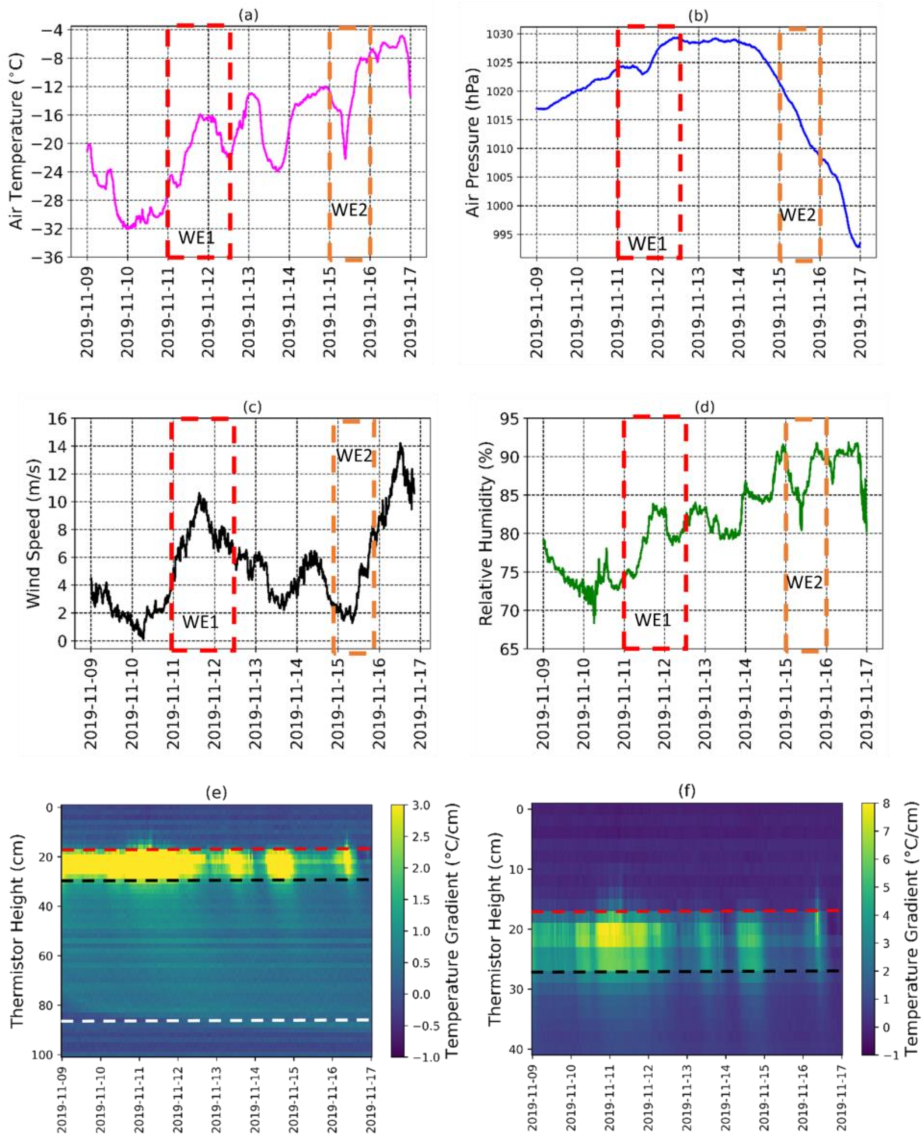

Figure 3: Line plots show daily, 10-min averaged 2~~-~~m (a) air temperature, (b) air pressure, (c) wind speed and (d~~b~~) relative humidity, recorded by the MET tower between 9 and 16 November. 2D color~~Surface~~ plots show DTC-derived hourly-averaged temperature gradient of (e~~c~~) near-surface, snow, sea ice and ocean; and (f~~d~~) sub-section of panel (e) showing the snow volume from~~volume snow volume from~~ the RSS. Yellow represents larger temperature gradients within the snowpack. Dotted red, black and white lines represent approximate locations of the estimated air/snow, snow/sea ice and sea ice/ocean interfaces. ~~Yellow pixels represent snow volume.~~ DTC temperature sensors are spaced by~~ every~~ 2 cm, with the top 20 cm representing the height above the air/snow interface~~ distance between the first sensor located above the air/snow interface and at the air/snow interface~~. Red and orange boxes in (a) to (d) indicate WE1 and WE2 windows. Note the different temperature gradient scales for (e) and (f).

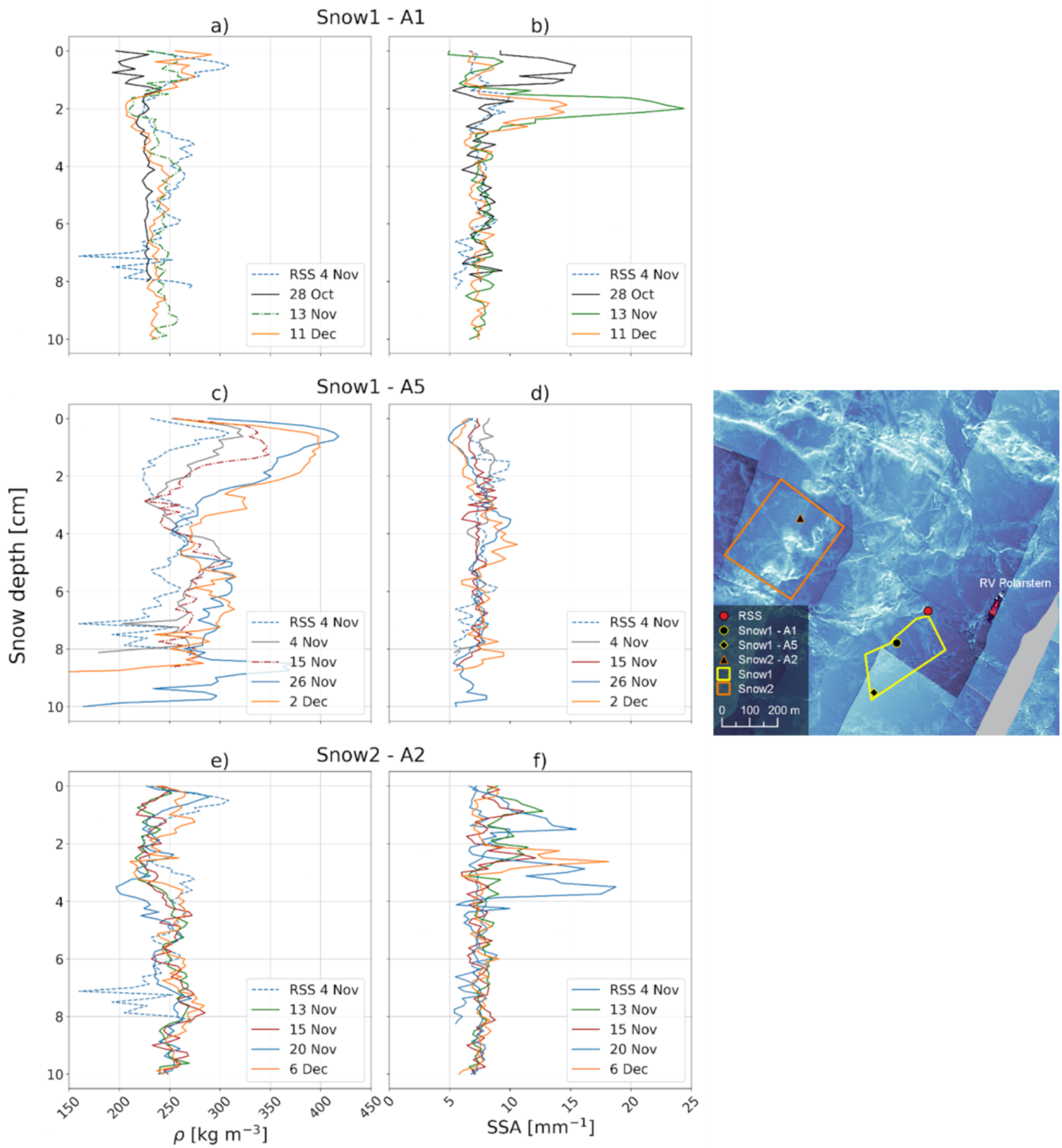
Snow1 - A1
a)
b)
RSS 4 Nov
28 Oct
13 Nov
11 Dec
Snow1 - A5
c)
d)
RSS 4 Nov
4 Nov
15 Nov
26 Nov
2 Dec
Snow2 - A2
e)
f)
RSS 4 Nov
13 Nov
15 Nov
20 Nov
6 Dec
Snow depth [cm]
ρ [kg m⁻³]
SSA [mm⁻¹]
RV Polarstern
RSS
Snow1 - A1
Snow1 - A5
Snow2 - A2
Snow1
Snow2
0 100 200 m

Figure 4: The upper 10 cm of the horizontally averaged density and SSA profiles of the snowpack over time derived from the SMP force signals (where the average consists of 5 SMP profiles at each location), from (a & b) Snow 1 - A1, (c & d) Snow 1 - A5, and (e & f) Snow 2 - A2 locations. In each subplot, the horizontally averaged profile measured at the RSS measured on 4 November 2019 is illustrated~~shown~~ for comparison (blue dashed line). Map shows the immediate surroundings of the study site. The RSS is illustrated~~shown~~ with a red dot, colored lines show the extent of Snow1 and Snow2 sites, and SMP locations within these sites in colored shapes. The background is preliminary quicklook-processed surface elevation data from the airborne laser scanner, where the whiter colors indicate high elevations of ≥ 2 m

During WE1, the ~~surface~~ air temperature increased ~~on 11 November~~ from ~ -32°C (0800 UTC) to ~ -16°C (~ 2000 UTC) (Figure 3a). During WE2, ~~surface~~ air temperature increased to ~ -4°C by ~ 1800 UTC ~~on 15 November~~ and remained relatively warm until the end ~~of WE2~~ (Figure 3a). These changes clearly influenced the temperature gradients across the snowpack, with a~~measured by the DTC thermistor string (Figure 3e & f). A~~ large, vertical temperature gradient of >7~~3~~°C/cm ~~was produced~~ early in WE1~~, whereas the average gradient~~ decreaseing~~d~~ ~~by half~~ to ~ 3°C/cm during WE2 (Figure 3f~~c &~~ d). S~~During this period, s~~now temperature gradients consistently exceeded 2.5~~0.25~~°C/m, suggesting temperature gradient-driven hoar metamorphism was occurring throughout the snowpack (e.g. Colbeck, 1989).

SMP-derived density and SSA profiles demonstrate~~measured at all Snow1 and Snow2 locations exhibit~~ an increase in density and decrease in SSA ~~density and SSA~~ over time~~, respectively~~, in ~~from~~ the uppermost (2 cm) snow layers (Figure 4). ~~An increase in snow density in the uppermost 2 cm layer in the snowpack is visible for all three locations (left panels).~~ The density increase at Snow 1 - A5 until 26 November is most distinct. The density and SSA profile from the RSS measured on 4 November correlates well with those from Snow1 and Snow2, indicating representative snowpack ~~evolution~~ conditions between RSS and Snow 1 and 2 locations. The average density change of the upper 2 cm between the last and the first measurement at each location is +30.7 kg/m^3 at Snow 1 - A1, +79.3 kg/m^3 at Snow 1 - A5, and +22.9 kg/m^3 at Snow 2 - A2 (Figure 4). The SSA change is -2.0 mm^{-1} at all snow pit locations (right panels). Based on the 5 SMP profiles, we computed the snow depth ~~changes~~, finding ~~where we found~~ a slight increase over time for each location. At Snow 1, the increase was 1.7 cm and 0.2 cm at A1 and A5 locations, respectively, with a 1.2 cm increase in snow depth from the A5 location, sampled between 4 and 26 November. At Snow2 - A2, the overall increase was 0.3 cm, with a 0.8 cm increase recorded between 13 and 20 November.

The increase in surface snow ~~surface~~ density is typical for strong wind action on the snow (Lacroix et al., 2009; Savelyev et al., 2006). W~~Substantially w~~armer air temperatures during the observed wind events, compared to pre-wind conditions (Figure 2) also increase the likelihood for snow grains to sinter (e.g., Colbeck, 1989), favouring snow surface compaction. A~~n~~ SSA decrease indicates the reduction in surface area, caused by rounding~~caused rounding~~ of snow grains, followed by sintering during ~~by the breakup of snow particles during~~ wind transport (King et al., 2020).

3.1.3 Snow Surface Topography Dynamics

3.1.3.1 Snow bedform evolution

Wind events caused~~WE1 and WE2~~ ~~resulted in~~ a dynamic evolution of snow bedforms~~ features~~ in the radar scan area (Figure 5 and Supplemental Video 1). On 9 and 10 November (Figure 5a & b), the snow cover was~~is~~ characterised by bedform features (white stars)~~ in negative θ_{az} sectors~~, as well as crag and tail features and patterned tail markings ~~in positive θ_{az} sectors~~ (yellow star), both typically found on relatively level sea ice (Filhol & Sturm, 2015).~~.~~ The major axis of these bedforms is predominantly oriented parallel to the radar azimuthal scan direction. ~~These features are typically found on relatively level sea ice (Filhol & Sturm, 2015).~~

Between 11 November until ~ 0800 UTC on 12 November, winds blew snow both radially and azimuthally relative to the radar scan area at different times. Because the radar sled forms an aerodynamic obstacle, the snow drifted unevenly in the lee of the sled (red star in Figure 5c-f and Supplemental Video 1). While snow depth could not be measured in~~within~~ the radar~~'s~~ scan area~~ without disturbing the snow~~, considering the 30 cm radar sled height, snow drifts covering the edges of the sled indicate an increase in snow depth to > 30 cm directly in front of the radar. Blowing snow buried the existing bedforms from 9 and 10 November, creating a new drift with its major axis oriented parallel to the azimuthal radar scans ~~direction~~ ~~positive θ_{az} sectors~~, and with an increasing slope (greater snow depth) with increasing θ_{inc} (black star in Figure 5e-g). A new sastrugi also developed as a result of WE1~~ in the negative θ_{az} sectors~~ (brown star in Figure 5e & f). WE2 on 15 November caused the rapid formation of two new snow drifts~~ in the negative θ_{az} sector~~, oriented parallel to the prevailing wind direction (purple stars in Figure 5g). A small pit-like feature also formed in the depression between the two drifts (dark blue star in Figure 5g), while the drift (black star) that formed during WE1 is still visible~~ in the positive θ_{az} sectors~~.

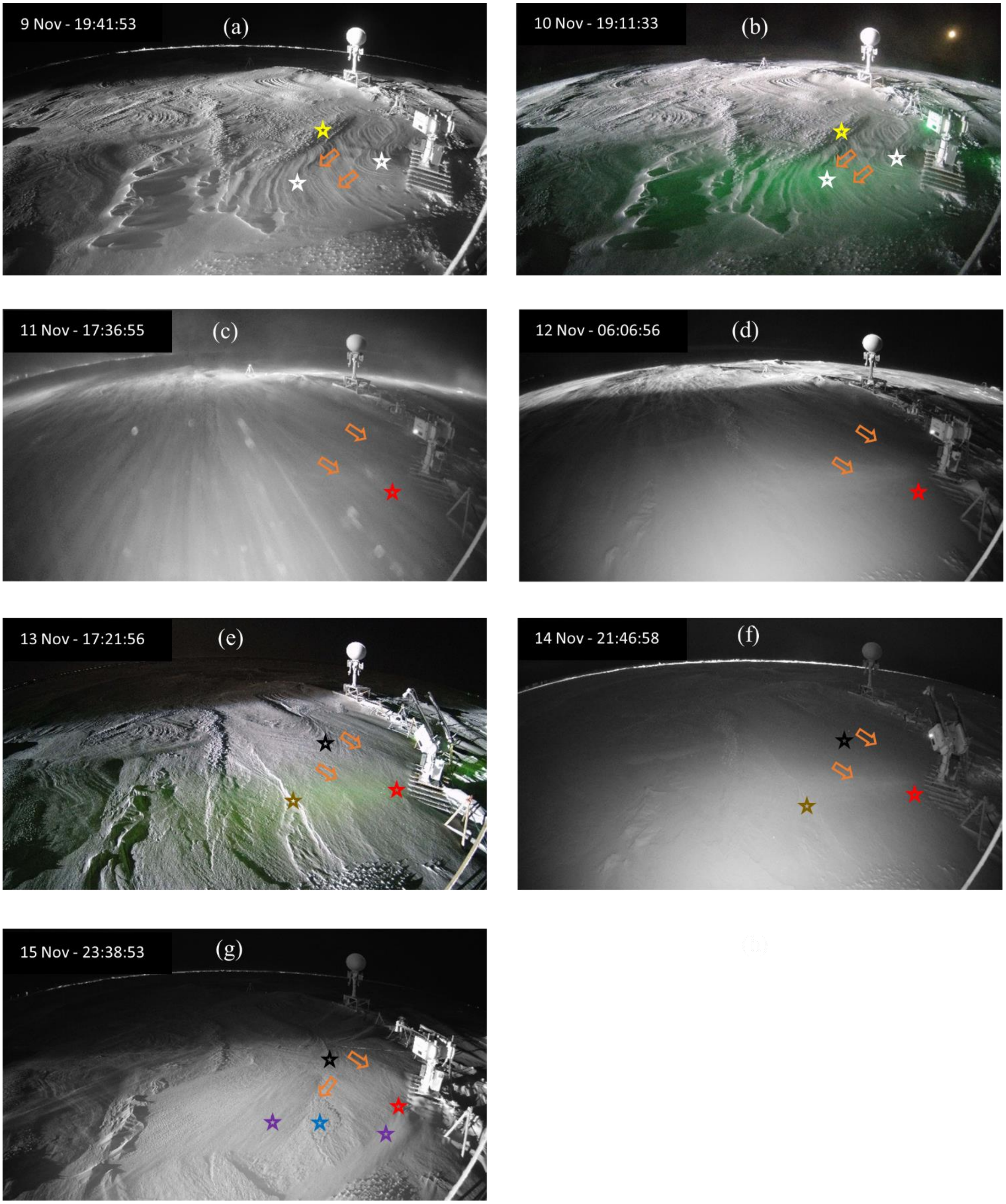

Figure 5: I~~CCTV i~~mages of~~from~~ the RSS scan area between (a) 9 November and (g) 15 November. I~~CCTV i~~mages were selected during times of the day when the ship's floodlight was illuminating the scanning area. The KuKa radar is on the far right on the images, while an

L-band Scatterometer is on the upper right. Coloured stars represent major snow bedforms within the KuKa radar scan area, while orange arrows show the orientation of the bedforms in response to prevailing wind direction. All times are UTC.

3.1.3.2 Snow Surface Heights from TLS

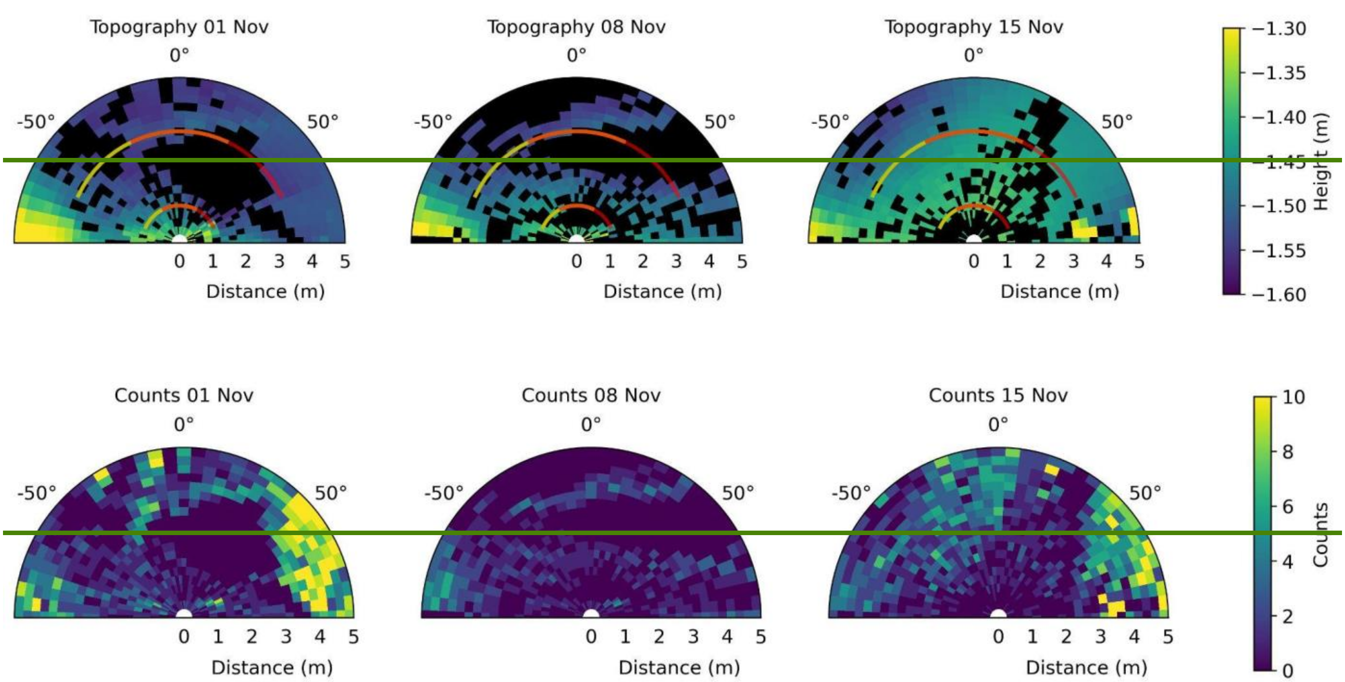

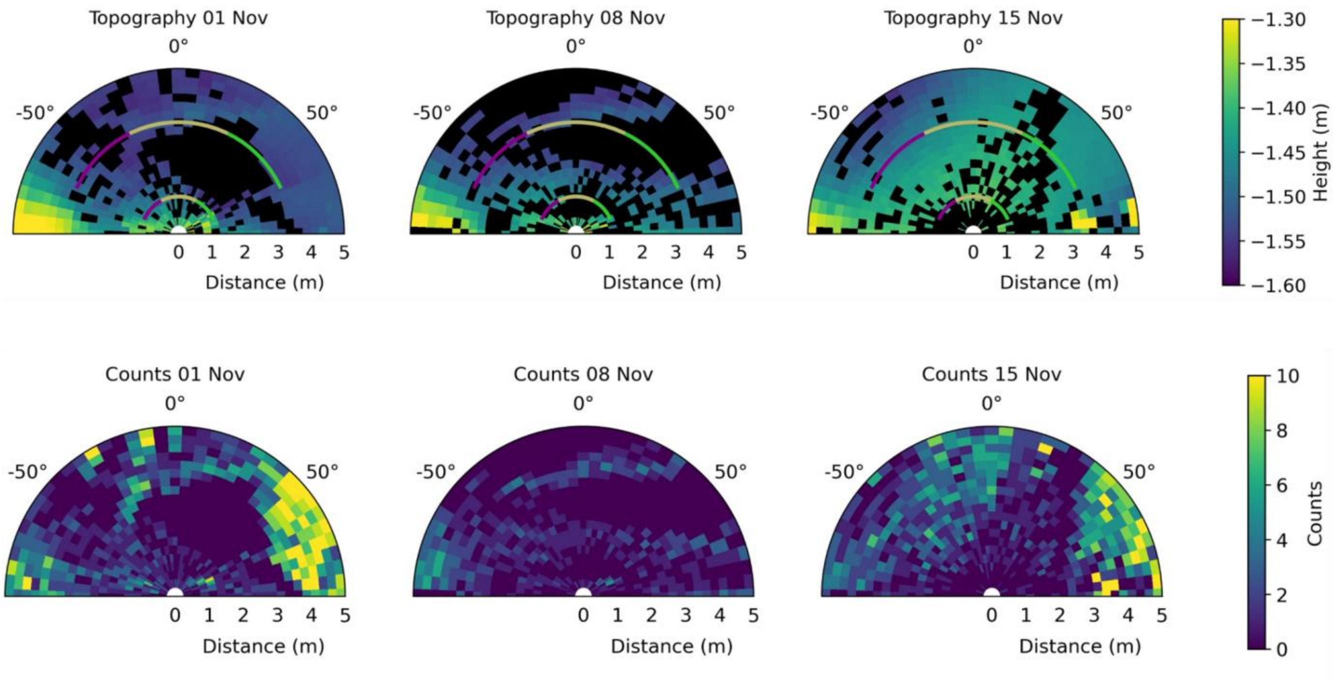

Figure 6: TLS data (plan view) from 1, 8 and 15 November, from -90° to + 90°, where the angle indicates the azimuth of the radar positioner, and radial horizontal distance measured from the centre of the radar pedestal. The top panels show the topography as measured downwards (increasing negative) from the middle of the radar antenna arms. Black indicates no data recordings in that bin. Projections of the centres of the radar scan area are illustrated~~shown~~ for 0° and 50° radar incidence~~inclination~~ angles between -65° to + 65° azimuth range, superimposed on the TLS data in magenta and green~~yellow and red~~ for radar observations, respectively, and buff ~~orange~~ where the two overlap, as per Figure 1. The bottom panels indicate the number of TLS data points within each bin. Surface depressions resulting in 0 counts in the TLS data are due to obscuration by adjacent high areas due to snow/sea ice topography and human-made objects, as viewed from the TLS's oblique viewpoint some distance away.

The TLS-derived snow surface height data from 1, 8 and 15 November are illustrated~~shown~~ in Figure 6 along with superimposed green~~red~~, buff~~orange~~, and magenta~~yellow~~ lines, indicating the centres of the radar scan area. Data from 1 November are included for context (left panel), indicating that the surface topography was similar to 8 November (middle panel). The TLS data illustrate~~show~~ considerable surface height variability within the radar scan area between 8 and 15 November, with snow surface height increasing (middle and right panel), as also indicated by the raised snow drift (black star in Figure 5e-g) at approximately 0° to 45° azimuth in the CCTV images.

3.2 Radar Waveforms

Figure 7 shows the temporal progression of Ka- and Ku-band radar waveforms at nadir, overlaid with spatially coincident TLS-derived surface heights and averaged into individual 5° azimuth sectors. ~~The TLS data and the waveforms are both averaged into individual 5° azimuth sectors, with the highest peak power overlaid in blue.~~ In the supplement, we provide an animation (Supplemental Video 2) that includes all radar data from~~obtained during~~ the two wind events, whereas here, we show ~~we show whereas here,~~. ~~In this section, we only show~~ ~~and discuss~~ four ~~date/~~time frames to illustrate the radar response. As TLS data were acquired~~gathered~~ weekly, there are only these data available to overlay; in addition, as relatively few data points were available for 8 November, we also show data from 1 November - before the ~~snow redistribution during the~~ wind events.~~, All~~ TLS data from all three dates are overlaid~~are shown overlaid~~ on all KuKa radar plots to demonstrate the time evolution of air/snow interface elevations in the two datasets~~!~~.

Prior to WE1, radar waveforms ~~from 9 and 10 November (top left and right panels in Figure 7)~~ remained stable, with only small power variations ~~in each azimuthal bin~~ over time. The ~~radar~~ peak power at VV and HH generally corresponds to the air/snow interface in most θ_{az} bins, as also confirmed by ~~detected by the radar corresponds to~~ the TLS-derived heights ~~detected by the TLS on 1 and 8 November~~.~~,~~ ~~indicating that both Ka- and Ku-band frequencies detect the air/snow interface as the dominant scattering surface at VV and HH in most~~ ~~θ_{az}~~ ~~bins.~~

A lower scattering interface is also visible at ~ 20 to 40 cm below the air/snow interface, especially prominent in the HV data in both frequencies, but also visible in the VV and HH data. The range values indicated in the radar waveforms are based on the speed of light in free space. Correcting for a reduction of 80% for snow (Willatt et al., 2009), the lower interfaces lay ~ 16 to 32 cm below the air/snow interface. To better understand this, we consider the HV waveform ~~characteristics~~ and local snow depth. Snow depth measured behind the ~~KuKa radar~~ scan area during 4 and 14 November varied between 21 and 29 cm ~~(not illustratedshown)~~. ~~Note that these measurements were not taken within the radar scan area close to the instruments to not disturb the radar measurements, and therefore, snow depth in the radar scan area may differ (see also Figure 6 for snow height variability). The range values indicated in the radar waveforms are based on the speed of light in free space, and the speed of propagation of the EM radiation would reduce to approximately 80% of that value in the snow (Willatt et al., 2009). Taking this correction into account and assuming similar snow depths at nadir, the lower interface in the waveforms lay ~ 16 to 32 cm below the air/snow interface.~~ Based on the very small amount of radiation scattered from larger ranges, negligible penetration ~~considering little penetration~~ of Ku- and Ka-band signals into sea ice (Fung et al., 1994), and the consistency with local snow depth, ~~we can conclude that~~ this interface in the HV data is very likely ~~is~~ the snow/ice interface. A small amount of returned power~~radiation~~ is expected from ~~ranges~~ beyond due to~~this interface caused by~~ snow and ice backscattering from the perimeter of the 30-50 cm radar scan area and sidelobes.

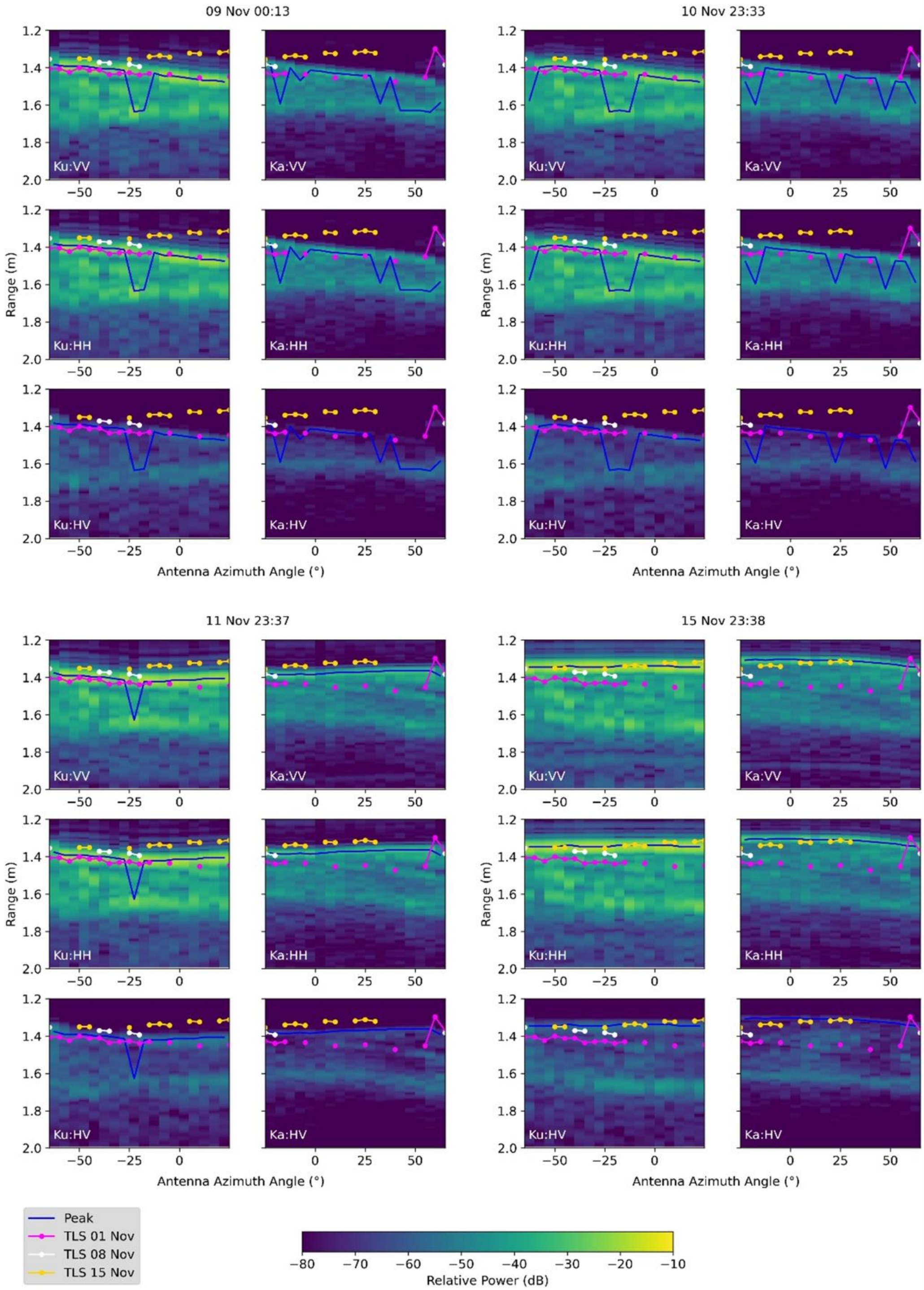

09 Nov 00:13
10 Nov 23:33
11 Nov 23:37
15 Nov 23:38
Ku:VV
Ka:VV
Ku:HH
Ka:HH
Ku:HV
Ka:HV
Range (m)
Antenna Azimuth Angle (°)
Peak
TLS 01 Nov
TLS 08 Nov
TLS 15 Nov
Relative Power (dB)

Figure 7: Progression of Ka- and Ku-band radar power-depth profiles at nadir between -65° to +25° (Ku-band) and -25° to +65° (Ka-band) (azimuth ranges following Figure 1(e) and (f)). Range (y-axis) is given from the antenna phase centre, and the antenna azimuth angles (x-axis) are the angles for that individual antenna. The highest power peak (averaged across all polarisations) is indicated with a blue line, and the surface height in the spatially coincident TLS data is superimposed on top (coloured circles).

During WE1, radar waveforms at nadir ~~in Figures 7 and 8~~ show that the peak power at the air/snow interface shifted upwards due to snow deposition at ~ 1800 UTC on 11 November (Figure 5c). This is followed by a snow scouring/erosion event, ~~which is~~ seen in the downward movement of the peak power (Supplemental Video 2), followed by~~and then~~ a second deposition event at approximately 0800 UTC on 12 November (Figure 5d)~~, which again sees~~ and upward movement of the peak power (Figure 8). It is interesting to note that the Ka- and Ku-band scattering can still be seen from the previous air/snow interface on~~from~~ 9 and 10 November (yellow arrows on Figure 8), as well as from the snow/ice interface, more prominent in the Ku-band. After WE1, the new air/snow interface remains the dominant scattering surface for all polarizations and θ_{az} sectors.

During WE2, after accumulation of newly redistributed snow, the air/snow interface moved upwards to a closer range from the antenna phase centre (bottom right panel in Figures 7 and 8). Scattering from the previously detected air/snow interface (corresponding to the TLS data from 1 and 8 November) is still visible in both Ka- and Ku-band data (Figure 8). In addition, the air/snow interface from 11 November remains visible in the Ka-band data in all polarisations (bottom left panel in Figure 7).

Next, we examined the highest amplitude peak ~~(under which the backscatter is calculated)~~ at nadir, and how this varies with frequency and polarisation, through time. Prior to WE1, ~~depending on the θ_{az} sector,~~ the highest power peak ~~fluctuated between~~ originated from both~~the~~ air/snow and snow/ice interfaces at both frequencies (top panels in Figure 7), suggesting variability in snow density (Figure 4) and surface topography (Figure 5) across ~~the θ_{az} sector within~~ the ~~nadir~~ scan area. During and after WE1 and WE2, the highest peak power remains almost always at the air/snow interface for both frequencies (bottom panels in Figure 7). This means that the backscatter values in the following Figures 8 to 10 correspond to the air/snow or snow/ice interfaces, depending on the θ_{az} sector and θ_{inc}.~~,; i.e., changes in backscatter could correspond to scattering from different interfaces,~~ rather than a change in backscatter from one interface. ~~-~~The TLS and radar waveforms also indicate a ~ 2-5° slope in the radar scan area especially at nadir (See Figures 6 and 7). Sloped surfaces of 2-5° will significantly affect the total backscatter amplitude ~~magnitude~~. However, since surface scattering is the dominant scattering mechanism at nadir, slightly sloped surfaces observed from the radar scan area likely do not affect the relative distribution of scattering between the air/snow and the snow/ice interfaces.

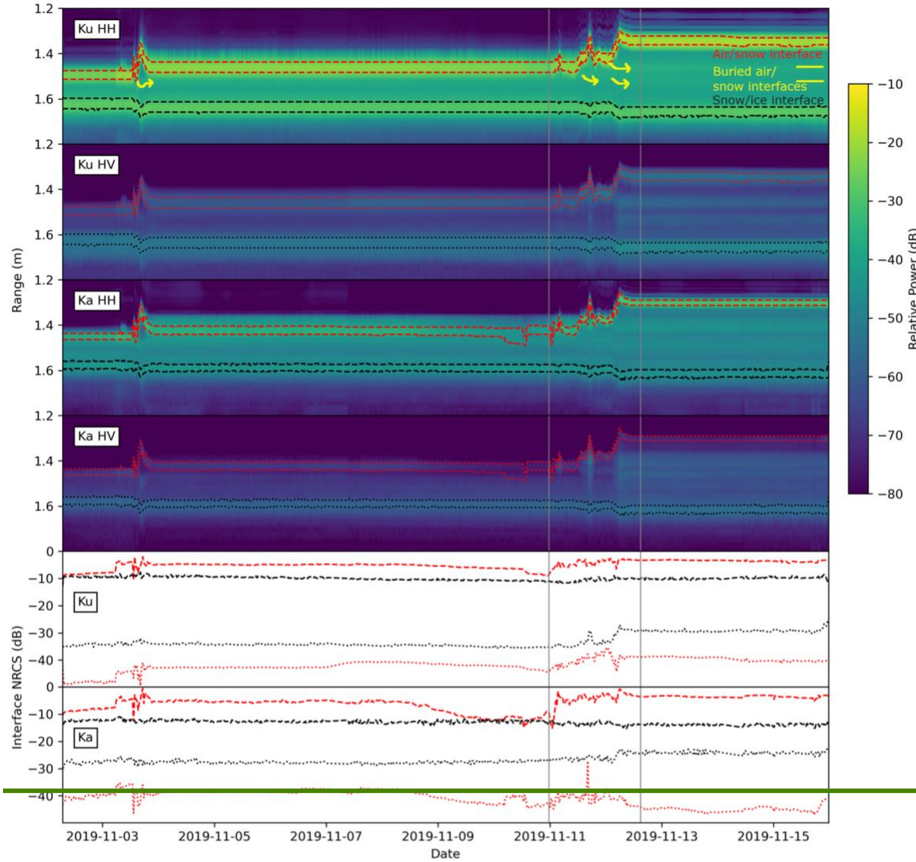
Ku HH
Ku HV
Ka HH
Ka HV
Air/snow interface
Buried air/
snow interfaces
Snow/ice interface
Range (m)
Relative Power (dB)
Ku
Ka
Interface NRCS (dB)
2019-11-03
2019-11-05
2019-11-07
2019-11-09
2019-11-11
2019-11-13
2019-11-15
Date

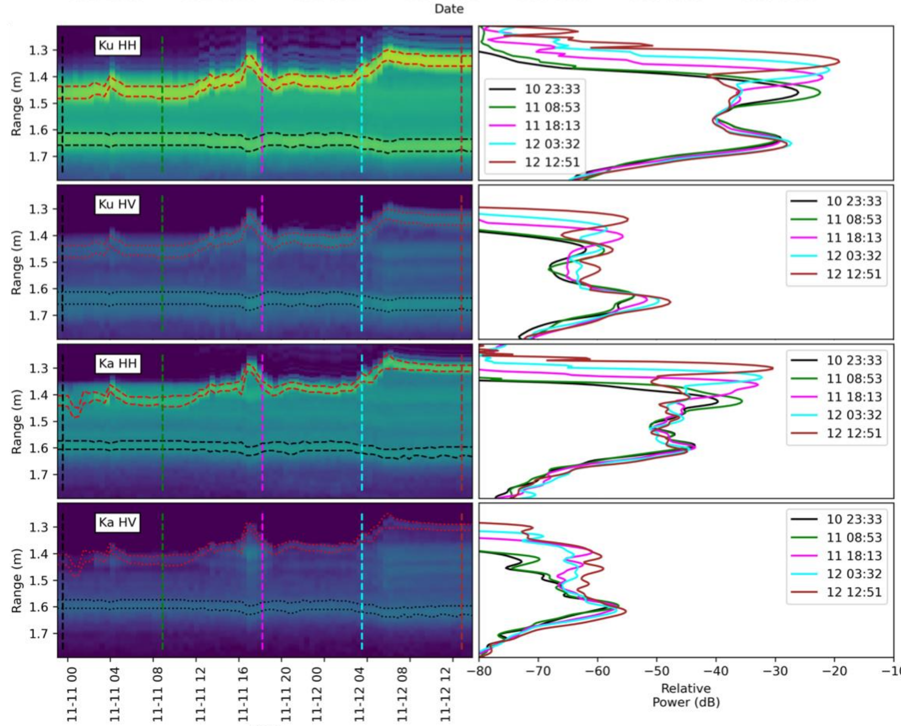
Ku HH
Ku HV
Ka HH
Ka HV
Range (m)
10 23:33
11 08:53
11 18:13
12 03:32
12 12:51
11-11 00
11-11 04
11-11 08
11-11 12
11-11 16
11-11 20
11-12 00
11-12 04
11-12 08
11-12 12
Date
Relative
Power (dB)

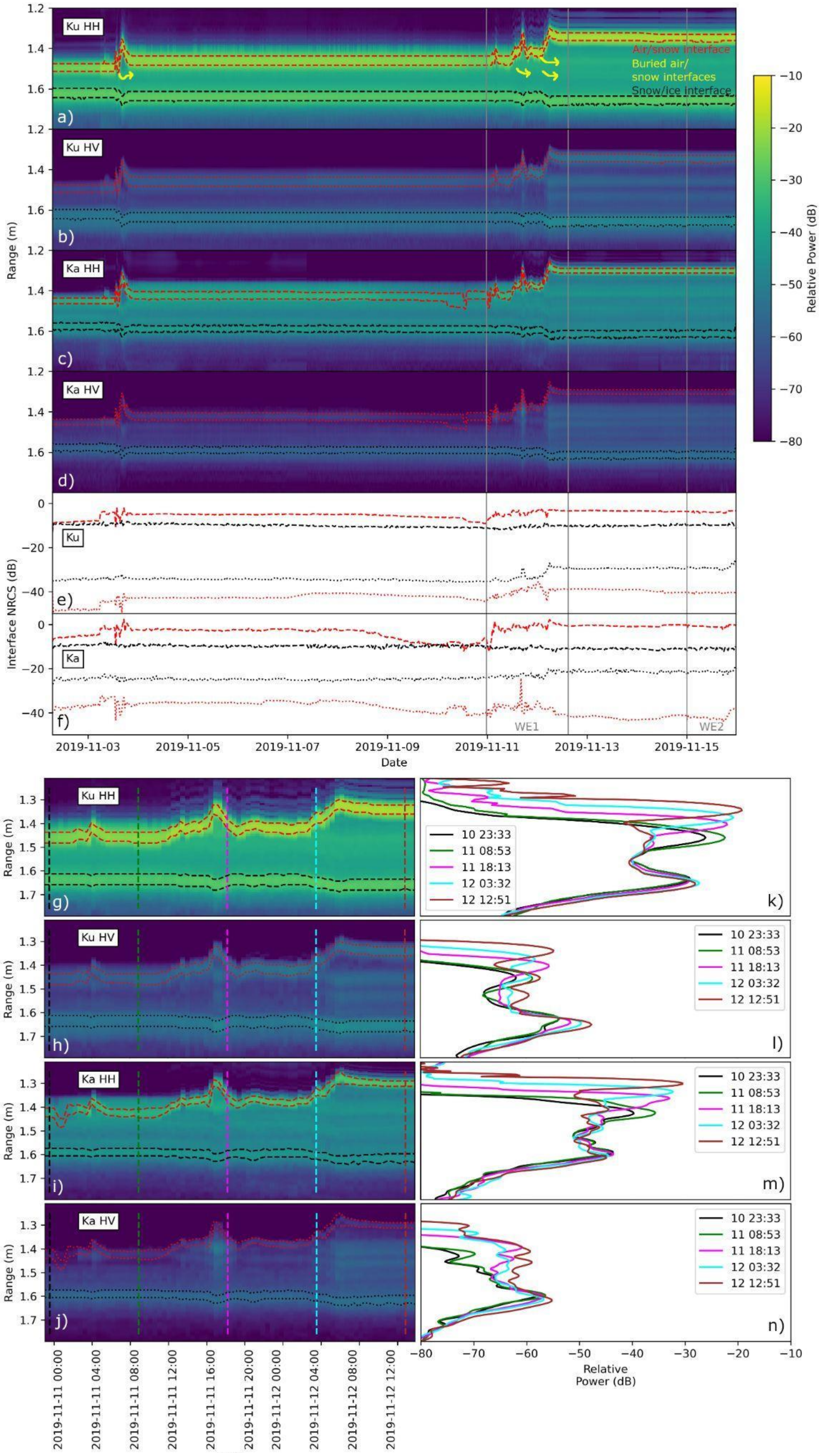
Ku HH
Air/snow interface
Buried air/
snow interfaces
Snow/ice interface
a)
Ku HV
b)
Ka HH
c)
Ka HV
d)
Range (m)
Relative Power (dB)
Ku
e)
Ka
f)
Interface NRCS (dB)
WE1
WE2
2019-11-03
2019-11-05
2019-11-07
2019-11-09
2019-11-11
2019-11-13
2019-11-15
Date
g)
h)
i)
j)
k)
l)
m)
n)
10 23:33
11 08:53
11 18:13
12 03:32
12 12:51
Relative
Power (dB)
2019-11-11 00:00
2019-11-11 04:00
2019-11-11 08:00
2019-11-11 12:00
2019-11-11 16:00
2019-11-11 20:00
2019-11-12 00:00
2019-11-12 04:00
2019-11-12 08:00
2019-11-12 12:00
Date

Figure 8: Progression of the power-depth distributions over the commonly sampled area of the scan area between -25° and +25° ~~(-5 to +45 θ_{az} for Ku-band, and -45 to +5 θ_{az} for Ka-band)~~. The top panels a) - d) indicate the full time series from 2-15 November with the current air/snow~~, buried previous air/snow,~~ and snow/ice interfaces indicated in red and black, respectively. Sketched yellow arrows show how buried air/snow interfaces remain visible through time. Individual air/snow and snow/sea ice interface NRCS values are determined by integrating power between the red/black dashed/dotted lines, which cover the range bins where the power is within 2 dB from the air/snow and snow/sea ice interface peak. Time series of the interface NRCS values are illustrated~~shown~~ below the echograms (panels e and f)). The timings of WE1 and WE2 are indicated with grey lines and labels across panels a) to f). The bottom panels g) to j) show a temporal 'zoom in' of WE1. Panels k) to n)~~. Right~~ show line plots of the waveforms at the given times corresponding to the vertical dashed lines on the echograms in g) to j).

Figure 8 illustrates~~demonstrates~~ the effect of WE1 and WE2 on HH-polarized waveform shapes and~~at nadir using echoes averaged across the Ka- and Ku-band overlapping area. HH data~~ shows that the air/snow interface is always the dominant scattering surface in both frequencies. In the HV data, the snow/ice interface is the dominant scattering surface, but both interfaces are visible in both frequencies and all polarisations. Previous air/snow interfaces are also visible as in Figure 7. The ~~sketched~~ yellow arrows on the Ku-band HH plot show how the previous air/snow interfaces that remain visible when additional snow accumulates~~ on top and remain visible throughout the timeseries~~. These buried interfaces, along with the snow/ice interface, appear at greater range when covered with thicker snow due to the reduced wave propagation speed in snow relative to air, increasing the two-way~~twoway~~ travel time back to the radar receiver.

For the Ka- and Ku-band HH data, there are relatively small changes to the NRCS associated with the snow/ice interface (Figure 8e and f) and~~. However,~~ changes ~~to the NRCS~~ associated with the air/snow interface are much larger.~~;~~ P~~p~~rior to WE1, the Ka-band air/snow interface NRCS reduces from -5 to -10 dB before increasing during, and after~~following~~ WE1 to -3 dB. At Ku-band, a similar pattern is observed with the air/snow NRCS reducing from -5 to -8 dB, then increasing to -3 dB following WE1. M~~This indicates that m~~ost ~~of the observed~~ changes to ~~overall~~ NRCS from wind events~~during and after WE1 and WE2~~ relate to backscatter changes from the air/snow interface~~ and only minimally to the snow/ice interface~~. The Ka-band HV data show the air/snow interface NRCS decreasing prior to WE1, increasing during the wind events and then reducing to a lower value than previously, whil~~est~~ the Ku-band data show the air/snow interface NRCS increasing during the wind events and remaining higher than previously. The different behaviour at the two frequencies indicates that this could relate to roughness, i.e., the change in roughness is dependent on length scales. This is illustrated~~shown~~ by further detail in the waveform line plots which indicate how the waveform shape changed with more variability relating to the air/snow interface and snow above the snow/ice interface in both frequencies and polarisations. Both the Ka- and Ku-band HV show the snow/ice interface becoming brighter during the wind events and remaining brighter afterwards; we speculate that this may be related to temperature-gradient driven metamorphism of basal-snow.~~, however, we are not able to confirm whether temperature gradient-driven snow metamorphism caused this.~~

3.3 Radar Backscatter ~~and Co-Polarized Phase Difference~~

This section~~The waveform analysis described in Section 3.2 illustrates how the locations of the peak power evolved during WE1 and WE2. We now~~ focuses on the backscatter response from the overlapping area ~~by~~ using ~~analysing the~~ azimuthally-averaged Ka- and Ku-band backscatter time series at discrete θ_{inc}= 0°, 15°, 35° and 50°. Included ~~in the analyses~~ are radar echograms at θ_{inc}= 15° and 35° during WE1~~ over the -25° to +25° θ_{az} overlap area~~, to support backscatter interpretation~~ at higher θ_{inc}. Next, we make~~ 2D interpolations of the spatial radar response along θ_{inc} and across 5° θ_{az} bins over both Ka- and Ku-band scan area separately are also used to ~~and~~ analyse backscatter changes ~~and CPD variability~~ at specific times on 9, 11 and 15 November.

3.3.1 Azimuthally-averaged Backscatter

During pre-wind conditions, both Ka- and Ku-band backscatter are relatively stable~~ at all θ_{inc}~~ (Figure 9a & b). At nadir, VV and HH returns primarily originate~~s~~ from~~as surface scattering at~~ the air/snow interface. With higher values of θ_{inc} ~~increases~~, air/snow interface scattering decreases~~reduces~~ due to the~~strong~~ specular component of the backscattering not returning to the radar detector. The signal is therefore increasingly~~away from the radar and is~~ dominated by ~~, and secondarily from~~ snow volume scattering and incoherent surface scattering at the snow/sea ice interface. HV backscatter originates primarily from the snow/sea ice interface (top panels in Figure 7).

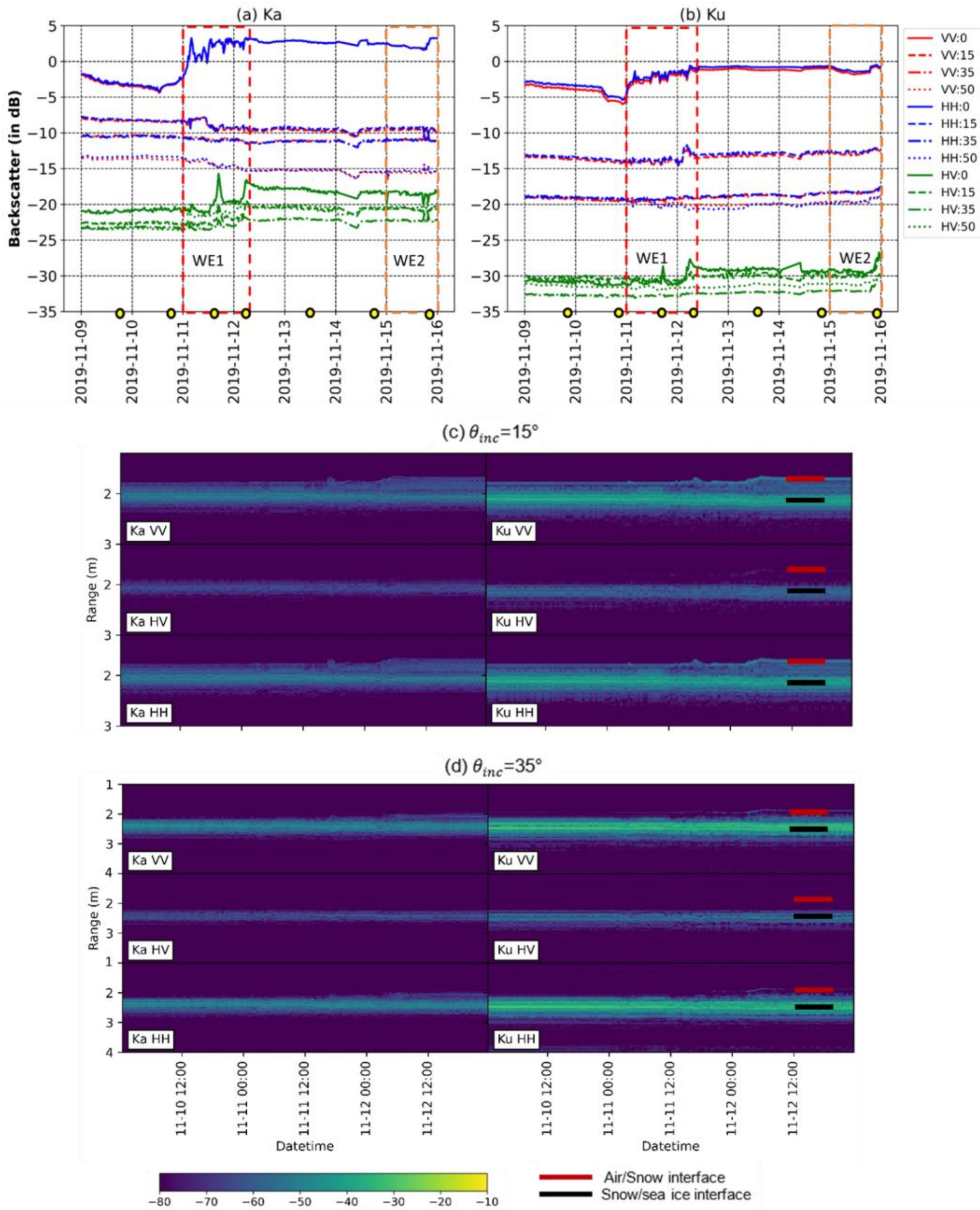

Figure 9: Azimuthally averaged (a) Ka- and (b) Ku-band backscatter at 0°, 15°, 35° and 50° incidence angles between 9 and 16 November, from the overlapping -25° to +25° θ_{az} area. Red and orange indicate the WE1 and WE2 time window. Yellow circles correspond to times of the day (in UTC) when the CCTV camera captured snapshots of radar scans. Panels (c) and (d) show time series of Ka- and Ku-band radar echograms at (c) θ_{inc} = 15° and (d) θ_{inc} = 35° during WE1.

During WE1, nadir backscatter increases significantly, with a greater Ka-band increase of ~ 8 dB (VV and HH), compared to a Ku-band increase of ~ 5 dB (VV and HH) (Figure 9a & b). The waveform analysis in Figures 7 and 8 indicates that the amount of scattering from the snow/sea ice interface changed very little during WE1, while the scattering contribution to the backscatter from the air/snow interface increased significantly due to ~~snow redistribution,~~ increasing ~~ncreasingmodifying the~~ snow density (Figure 4) and decreasing ~~surface/interface~~ radar-scale roughness (Figure 5). This increase is accompanied by additional VV and HH backscatter from the previous, now-buried air/snow interface ~~from the pre-wind conditions~~ (Figure 8). HV peak power shifts from the snow/sea ice interface to the air/snow interface and the buried within-snow interface (Figure 8). This is clearly seen in the two significant HV increases at nadir, by up to 5 dB (Ka-band) and by up to 4 dB (Ku-band) during WE1 (Figure 9a & b), coinciding with two short-term snow depositional events at ~ 1800 UTC on 11 November and around 0700 UTC on 12 November (Figure 5c & d and Supplemental Video 1).

At θ_{inc}= 15° and 35°, the peak power interfaces during WE1 are much less obvious than at nadir but do exist (Figure 9c & d). However, the bulk of the peak power moves from the air/snow interface to the snow/sea ice interface at all polarizations. The shifting of peak power from the air/snow interface to the snow/sea ice interface coincides with a decrease in Ka-band VV and HH backscatter by up to 2 dB at θ_{inc}= 15° due to reduced air/snow interface roughness. The effect is less at θ_{inc}= 35° due to the ~~reduced effect of air/snow interface roughness and potential~~ snow volume scattering becoming more dominant compared to surface/interface scattering at~~due to~~ the slanting cross section at more oblique angles. The waveform analysis shows that the relative contribution of the snow/sea ice interface, snow volume scattering and increased radar propagation delay due to increased snow accumulation becomes more important at shallow angles (Leinss et al., 2014) and the air/snow interface becomes relatively less prominent due to lower surface roughness after WE1. This feature is more observable in the HV data where the air/snow interface scattering is subtle, and the snow/sea ice interface is brighter, with potential snow and ice volume scattering ~~from the snow grains~~ (middle panels in Figure 9c & d). Ku-band at non-nadir incidence angles show negligible change in HV backscatter (more stable in HV at θ_{inc}= 35° and 50°), compared to Ka-band and pre-wind conditions (Figure 9b). It is expected that the HV backscatter is dominated by volume scattering processes and that volume scattering is more prominent in Ka-band ~~than in Ku-band~~ because of the shorter wavelength.

During WE2, Ka- and Ku-band backscatter at all θ_{inc} remains relatively stable (Figure 9a & b). Around ~ 2100 UTC on 15 November, a short-term snow depositional event (Supplemental Video 1) causes the Ka-band nadir backscatter to increase by ~ 2 dB. The Ka-band waveform analysis shows scattering contributions from the air/snow interface during the snow deposition and also from previously detected air/snow interface from 11 November (Figure 8 and lower right panels in Figure 7), causing the additional 2 dB increase. Similar to WE1, Ku-band backscatter at θ_{inc}= 35° and 50° ~~almost~~ remain~~remains~~ nearly the same throughout WE2 (Figure 9b). During WE2 it is likely that there is a slight snow surface roughness increase with a small nadir backscatter decrease and a small off-nadir increase. ~~Next, we show changes in the spatial varying backscatter and co-polarized~~

~~phase difference signatures within each 5° θ_{az} sector acquired at specific date/times during pre-wind conditions, WE1 and WE2.~~

3.3.2 Backscatter Response ~~and Co-Polarized Phase Difference~~ at $\Delta\theta_{az}$ = 5°

3.3.2.1 Change in Backscatter

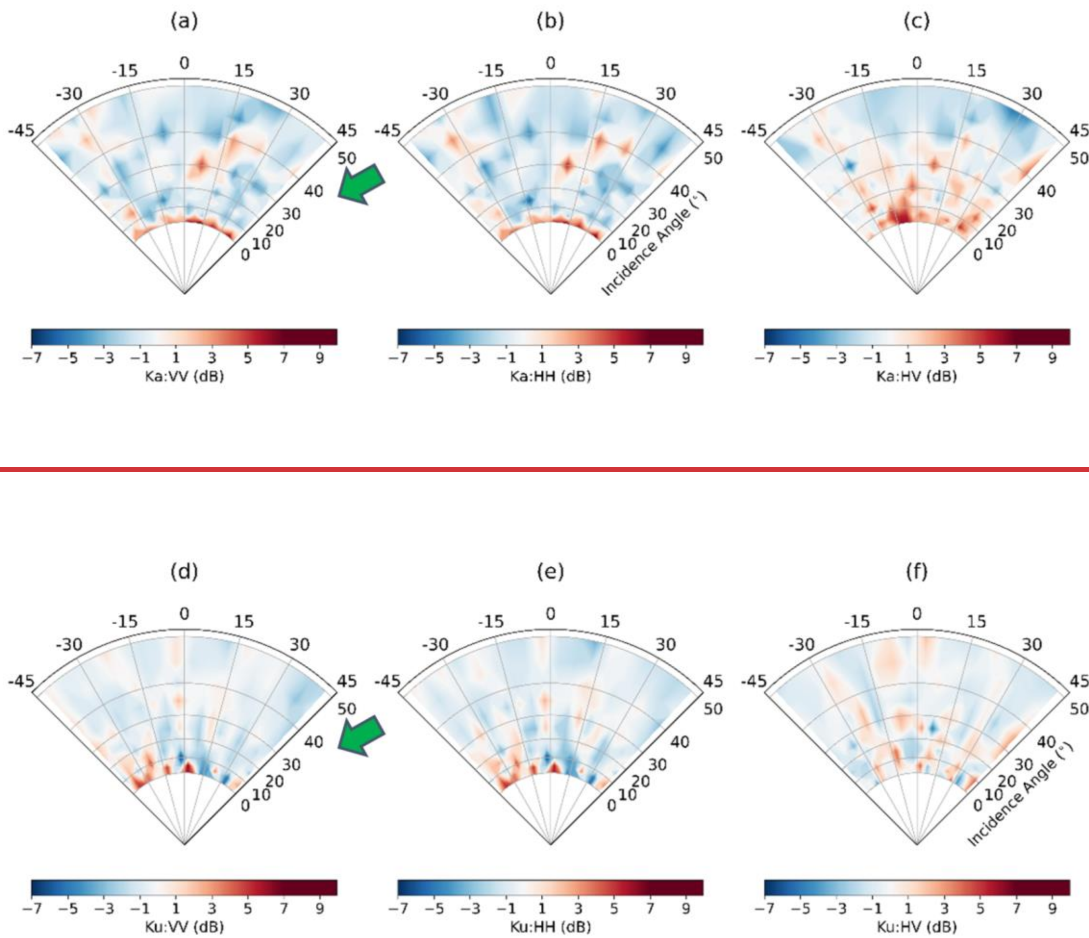

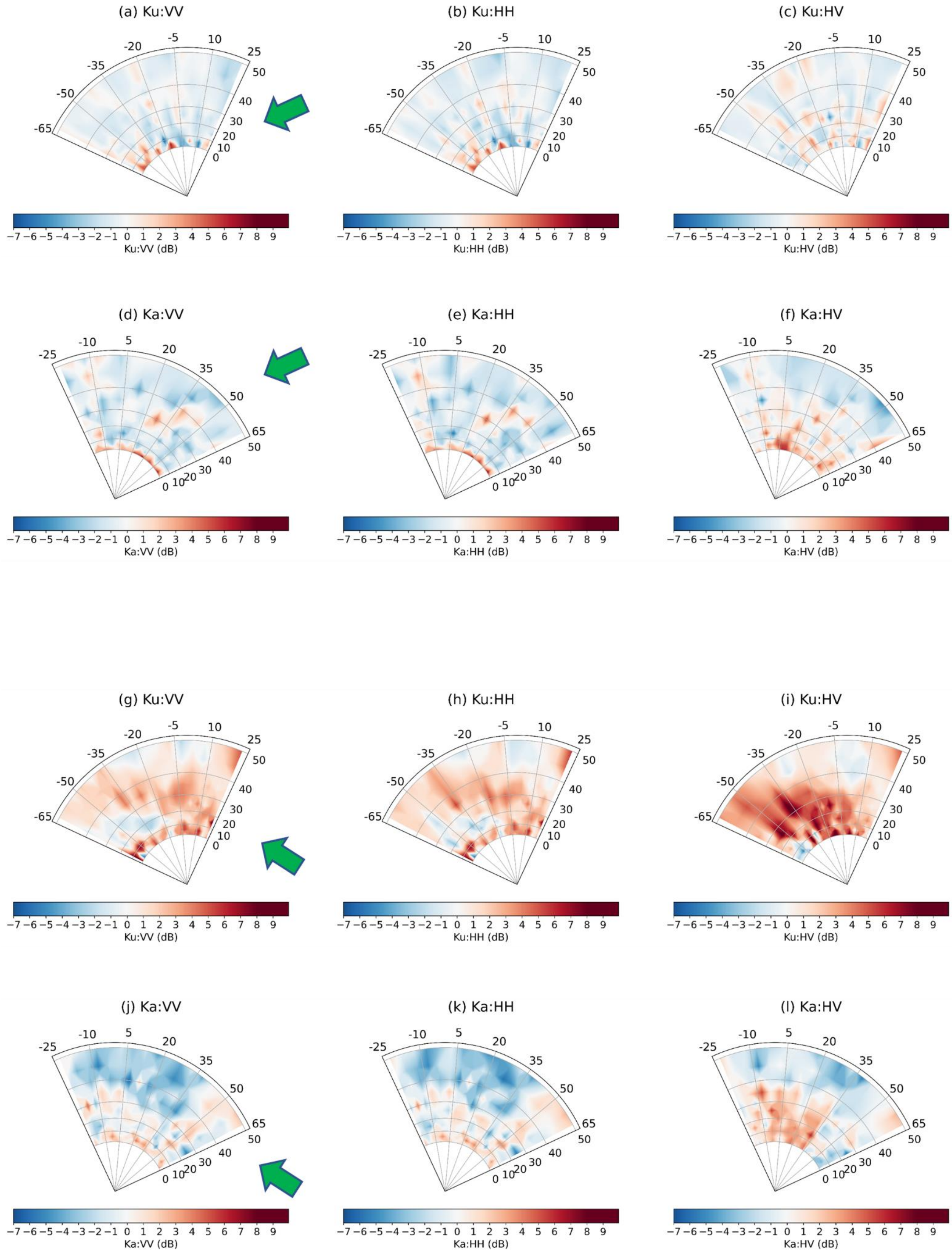
(a) Ku:VV
Ku:VV (dB)
(b) Ku:HH
Ku:HH (dB)
(c) Ku:HV
Ku:HV (dB)
(d) Ka:VV
Ka:VV (dB)
(e) Ka:HH
Ka:HH (dB)
(f) Ka:HV
Ka:HV (dB)
(g) Ku:VV
Ku:VV (dB)
(h) Ku:HH
Ku:HH (dB)
(i) Ku:HV
Ku:HV (dB)
(j) Ka:VV
Ka:VV (dB)
(k) Ka:HH
Ka:HH (dB)
(l) Ka:HV
Ka:HV (dB)

Figure 10: Polar plot panels (a) to (f) show the relative change in averaged Ku~~a~~- and Ka~~u~~-band backscatter at 5° azimuth sectors, as a function of θ_{inc} , between WE1 and pre-wind conditions, acquired on 11 (WE1) and 9 November, at 2337 UTC and 0013 UTC, respectively. Panels (g) to (l) show the same between windy conditions, acquired on 11~~5~~ (WE1~~2~~) and 15~~1~~ (WE2~~1~~) November, at 2337~~8~~ UTC and 2338~~7~~ UTC, respectively. Green arrows in (a) and (g) denote~~s~~ the prevailing wind direction on 11 and 15 November, respectively. The scan times also correspond to yellow circles in Figure 9 and CCTV images in Figure 5a & c. Note: The 11 November CCTV image in Figure 5c is acquired at 1736 UTC for image clarity showing blowing snow.

Changes in the spatial variation of the~~varying~~ backscatter within each 5° θ_{az} sector acquired at specific date/times during pre-wind conditions, WE1 and WE2 are shown in Figure 10. Compared to azimuthally-averaged Ka- and Ku-band backscatter (Figure 9), spatial variability in Ka- and Ku-band backscatter in response to wind events is evident at all polarizations and θ_{inc} ~~(Figure~~ 10~~s 10 and 11) in response to wind events~~. From pre-wind conditions to WE1, the most striking feature is the development of a drifted snow dune directly in front of the sled (red star in Figure 5) at θ_{inc} < 10°, which led to an increase in Ka- and Ku-band backscatter by up to 9 dB, at nadir throughout all θ_{az} sectors. Beyond θ_{inc} = 10°, the change in Ka-band VV and HH backscatter are primarily negative, with spatially heterogeneous areas of positive change, primarily in the ~~positive~~ θ_{az} sectors > 20° at θ_{inc} >~~=~~ 30° ~~(Figure 10(d) and (e)) and 40°~~. The change in Ka-band HV backscatter at θ_{inc} < 10° is more consistently positive at θ_{az} sectors < 0° ~~a θ_{inc} < 10° between 0° and -30° θ_{az} sectors~~, and it agrees well with the strong HV backscatter increase related to deeper snow ~~(Figure 9)~~ during the first snow depositional event that occurred halfway through WE1 on 11 November (Figure 5 and Supplemental Video 1).

WE2 produces a stronger response in Ka- and Ku-band backscatter across the θ_{az} sectors ~~(Figure 10 (g) to (l)11)~~, compared to WE1. Ka-band VV and HH backscatter change is primarily negative (up to ~~a reduction of~~ 7 dB) at θ_{inc} > 30°, while Ka- and Ku-band HV backscatter shows strong positive change (up to 9.5 dB) at θ_{inc} > 40°. Images in Figure 5~~CCTV images (Figures 5d-g)~~ and TLS scans from 8 and 15 November ~~acquired between WE1 and WE2~~ illustrate changes in surface heights, due to the drifts that formed towards the left side of the KuKa radar ~~in the negative θ_{az} sectors~~ (purple stars in Figure 5), and the deeper snow ~~this~~ appears to be captured by a strongly enhanced Ku-band HV response at θ_{az} sectors < 0° ~~(Figure 10(i)1f)~~. The large backscatter changes along these sectors ~~the negative θ_{az} sector~~ aligns with the wind direction also indicates change in snow topography from snow blowing entrained from behind the radar.

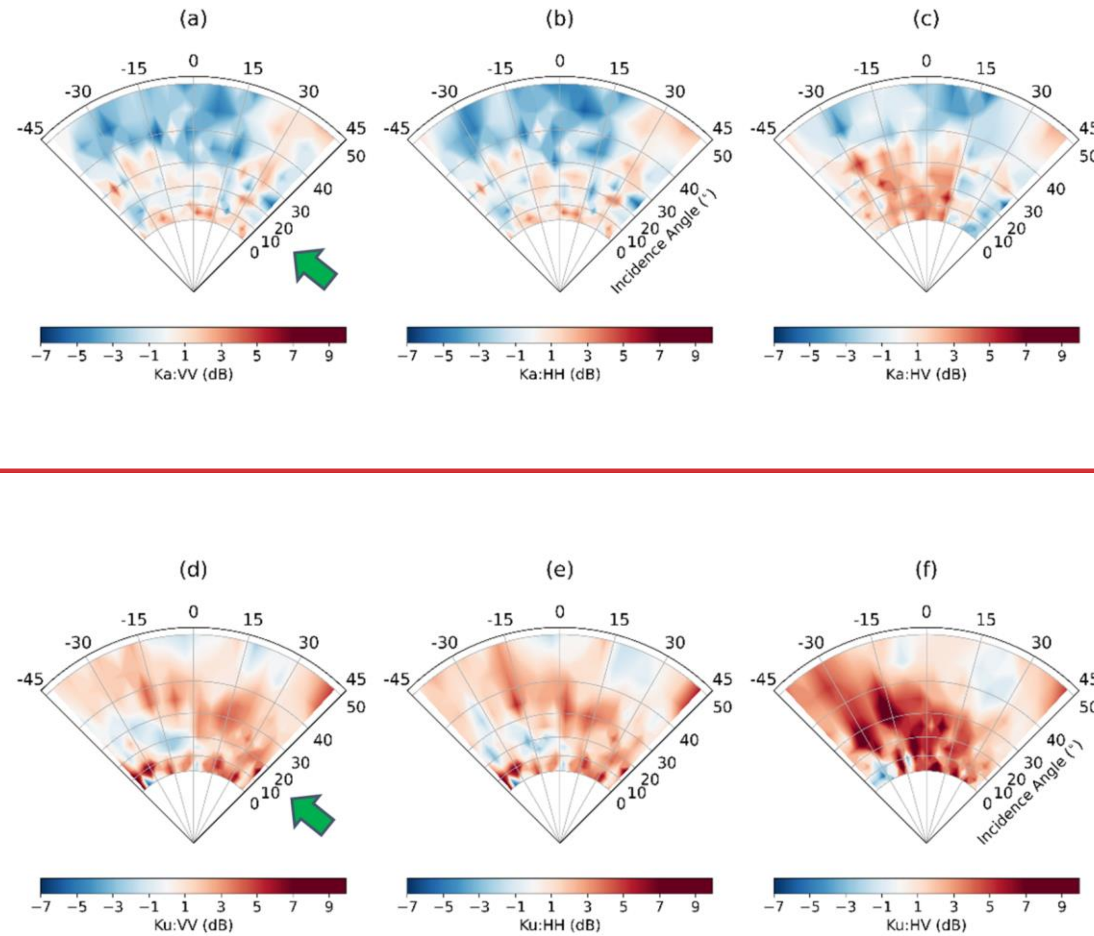

~~Figure 11: Polar plot panels show the relative change in averaged Ka- and Ku-band backscatter at 5° azimuth sectors, as a function of θ_{inc}, between windy conditions, acquired on 15 (WE2) and 11 (WE1) November, at 2338 UTC and 2337 UTC, respectively. Green arrow denotes the prevailing wind direction on 15 November. The scan times also correspond to yellow circles in Figure 9 and CCTV images in Figure 5c & g..~~

~~3.3.2.2 Co-polarized Phase Difference~~

~~Prior to WE1, Ka-band CPD is primarily negative and Ku-band CPD is positive (Figure 12a & b), suggesting stable snow metamorphism during pre-wind conditions. During WE1, Ka- and Ku-band CPD increase from pre-wind conditions at $\theta_{inc} <$ ~ 35°, in positive θ_{az} sectors (Figure 12c & d). This suggests a short-term wind effect on the snow structure, likely due to newly-deposited snow aligned with the prevailing wind direction (black star in Figure 5e). Also, the horizontal alignment of dunes or newly-deposited snow crystals would make new snow layers structurally anisotropic, causing a CPD increase (Leinss~~

~~et al., 2016). At $\theta_{inc} > 35°$ (Ka-band) and > 45° (Ku-band), the snow located in these sectors appears to have been minimally affected by the wind (Figures 5a-e and Supplementary Video 1). However, the cold temperatures prior to WE1 (Figure 3c & d) likely led to significant snow metamorphism in these incidence angle sectors, changing the snow structure alignment from horizontal towards vertical, causing the CPD to become negative (Leinss et al., 2016).~~

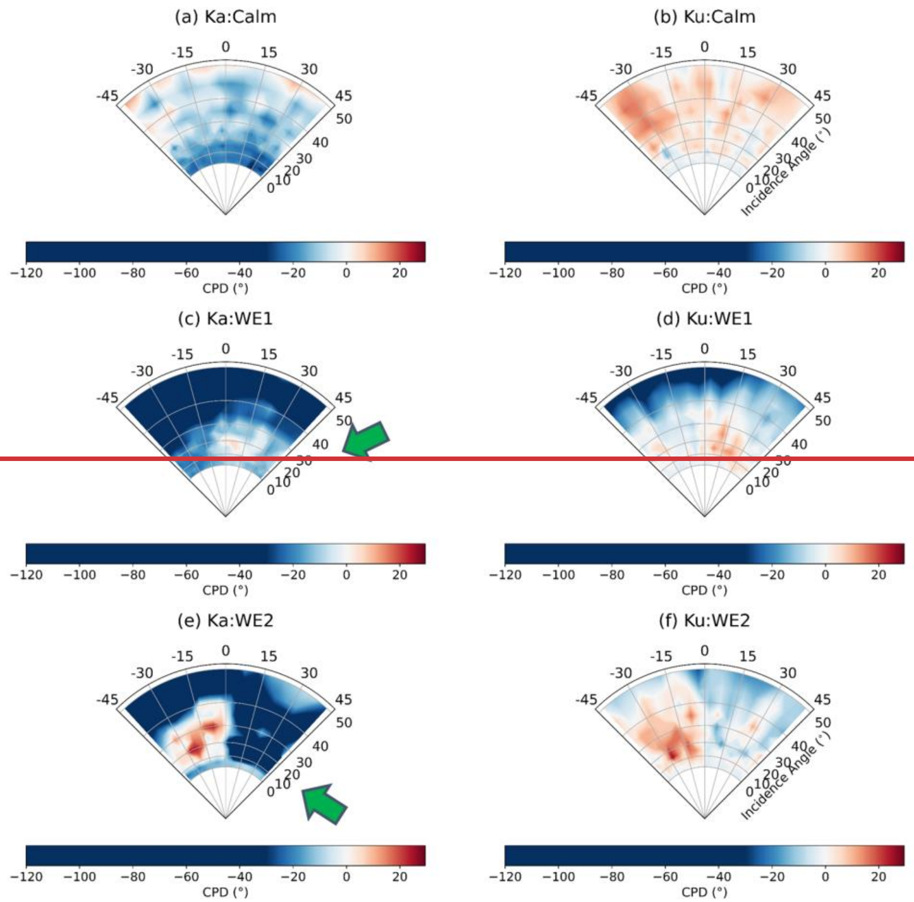

~~Figure 12: Polar plot panels show averaged Ka- and Ku-band co-polarized phase difference at 5° θ_{az} sectors, as a function of : (a) & (b) calm conditions on 9 November (~ 0030 UTC); (c) & (d) WE1 on 11 November (~ 1810 UTC); and (e) & (f) WE2 on 15 November (~~~

~~2338 UTC). Green arrow denotes the prevailing wind direction on 11 and 15 November. The scan times also correspond to yellow circles in Figure 9 and CCTV images in Figure 5.~~

~~During WE2, CPD shifts are increasingly negative in the positive θ_{az} sectors at all θ_{inc}, indicating minimal snow deposition in these sectors during WE2 (Figure 12e & f and Supplemental Video 1). Compared to Ku-band, CPD values are more negative in Ka-band in these sectors, due to its stronger sensitivity to continuous snow metamorphism throughout WE1 and WE2. Compared to WE1, in the negative θ_{az} sectors, Ka- and Ku-band CPD exhibits phase reversal and stronger positive shift at θ_{inc} < ~ 40° (Figure 12e & f). This is likely the result of additional snow redistribution and the resultant formation of two drifts in this sector (purple stars in Figures 5g, and Supplemental Video 1), and with the new snow having horizontal crystal alignment and corresponding phase shift and positive CPD values, stronger at Ka-band.~~

4. Discussion

4.1 Impact of Snow Redistribution~~Redistributed Snow~~ on Radar Signatures

Our analyses demonstrate that Ka- and Ku-band backscatter and waveforms are sensitive to wind-induced snow redistribution ~~at all polarizations, and incidence angles~~. During pre-wind conditions, the dominant radar scattering surface at nadir for both frequencies at the co-polarised channels switches between the air/snow and snow/sea ice interfaces depending on local variations in snow surface density and roughness. ~~while the~~ HV backscatter surface changes as a function of snow depth ~~the strength of the scattering response between these surfaces~~. This is illustrated~~shown~~ by the waveform analysis, with the range to the air/snow interface confirmed by georeferencing the radar and TLS data (Figures 7 and 8 and Supplementary Video 2), and the range to the snow/sea ice interface inferred from local snow depth measurements and the strong interface contrast evident in backscatter in the radar waveforms and the opposite changes (increase/decrease) in the nadir and off-nadir backscatter. Following WE1, the air/snow interface becomes the dominant scattering surface at nadir at all polarizations due to the smoothening of the snow surface combined with the increased snow surface density. At satellite scales, this may upwardly shift the retracked elevation and resulting sea ice freeboard retrievals by radar altimeters ~~when~~that assume ~~assuming that~~ the snow/sea ice interface is the dominant scattering surface.~~,~~ This would introduce an overestimating bias on the sea ice thickness estimate, however a number of other uncertainties are also at play in this process, meaning this may move the retrieval closer or further from the true value. Our surface-based findings are consistent with recent satellite-based work by Nab et al. (2023), who showed a temporary lifting of CryoSat-2-~~'s~~ derived radar freeboard in response to snow accumulation, but also higher wind speeds and warmer air temperatures. ~~Our results in this regard call for careful and therefore, warrants careful interpretation of waveforms and backscatter at nadir.~~ Due to snow surface smoothening, ~~A~~at non-nadir incidence angles, the relative scattering contribution of the snow/sea ice interface compared to the air/snow interface increases, and the air/snow interface gradually becomes invisible (Figure 9)~~. and therefore, our observations are crucial towards reliable interpretation of~~

~~These observations provide contextual information for reliably interpreting backscatter across all polarizations, incidence angles and azimuth ranges.~~

The Ku- and Ka-band radar backscatter is still sensitive to the presence of buried and historical air/snow interfaces within the snowpack (Figures 7-9), which indicates that snow density and/or surface roughness contrasts (Figure 4) existing prior to wind events continue to influence scattering even once additional snow is deposited ~~on top~~ (Figure 8). This is an important finding, because even if an interface is not the dominant scattering surface, it can affect the waveform shape and ~~consequently~~ assumptions about the surface elevation retrieved from airborne and satellite radar altimetry data when there is no a priori information on the snow geophysical history. In future studies, gathering TLS data on the snow surface roughness at high spatial (radar) and temporal (e.g., daily or hourly) resolution would provide valuable information on the role of roughness. In addition, collecting near-coincident measurements of snow density would provide information on the role of density affecting radar waveforms. We would therefore recommend collecting these coincident datasets in future similar studies.

The relatively small backscatter observed from the snowpack at θ_{inc}= 15° and 35° (Figure 9c & d) indicates dominant scattering away from the radar. At ~~Additionally, at~~ these angles, most of the backscatter is associated with the snow/sea ice interface, and that deeper snow is causing an increasing slant-range delay. ~~This absence of volume scattering change (due to wind-driven snow microstructural changes) at non-nadir θ_{inc}, in combination with the observed nadir sensitivity, suggests that surface scattering is the dominant changing scattering mechanism at nadir.~~ The air/snow interface is directly impacted by the wind, experiencing compaction to higher snow density and reduced ~~lower~~ surface roughness ~~changes~~ (Figures 4 and 5). The NRCS associated with the air/snow interface increased by more than 5 dB during and following the wind events (Figure 8). Thus, utilising time-series backscatter at both near- and off-nadir incidence angles may be useful for retrieving snow surface roughness and/or density changes, though it may be difficult to separate these variables.

This study does not replicate airborne- and satellite-scale conditions (e.g., beam geometry, snow cover and ice type variability on satellite-scales~~s (e.g. SAR scale), due to the experimental setup and scan area of the KuKa radar~~. Therefore, the waveform shape, return peak power and measured backscatter from the KuKa radar will be different from airborne and satellite radar altimeters and ~~spaceborne~~ scatterometers ~~or altimetersSAR~~. Also of note is the highly localised nature of the radar~~thelocalized KuKa radar~~ backscatter, which is a ~~two-scale~~ function of small-scale~~microscale~~ surface roughness combined with local θ_{inc} that includes some steep angles due to snow drifts and bedforms in the scan area. Even at nadir viewing geometry, the beam-limited KuKa radar scan area covers an angular range of 12-17° which is many ~~an~~ orders of magnitude larger than the beamwidth of a satellite altimeter's antenna and ~~larger still than~~two orders of magnitude larger the equivalent-beamwidth ~~the maximum θ_{inc}~~ of the altimeter's pulse-limited footprint, which for CryoSat-2 is around 0.1° (Wingham et al., 2006).

The relative dominance of coherent ~~coherent versus non-coherent snow and sea ice backscattering~~ ~~mechanisms~~ over non-coherent backscatter mechanisms can vary significantly within the ~~envelope of~~ KuKa~~'s~~ beamwidth alone~~between these incidence angles~~, with coherent reflections from near-specular~~smooth~~ surfaces dominating the radar response more easily at satellite scales (Fetterer et al., 1992). However, even from a satellite viewing geometry, a smooth ~~rough~~ air/snow interface should produce sufficient backscattering at Ku-band to modify the leading edge of the altimeter waveform response (Landy et al., 2019). The larger satellite footprints may also include ~~undeformed or deformed topography and~~ different ~~scattering~~ surfaces ~~not included in the KuKa radar scan area~~, such as pressure ridges, rafting and rubble fields, hummocks, ~~smoother~~ refrozen leads, level first-year sea ice ~~floes~~ and open water. The effects of small scale~~microscale~~ roughness, larger scale topography and sub-beamwidth~~local~~ θ_{inc} would combine in different ways for larger footprints, such as from satellites operating at large θ_{inc}, where the distribution of local θ_{inc} may be less extreme and the signal would be dominated by the smooth parts of the surface (e.g. Segal et al., 2020).

As mentioned~~discussed~~ earlier, the KuKa radar has a much higher vertical resolution than CryoSat-2 ~~(2.5 cm vs 46 cm)~~ and AltiKa ~~(1.5 cm vs 30 cm)~~. This means that although the individual interfaces would not be resolved in the satellite data, the waveform shape and hence retrieved elevation could be affected by current, recent (days), and historical (weeks or longer) timescales of wind-driven redistribution changes to the snow topography and physical properties. ~~Satellite altimetry sea ice~~ ~~Rr~~Retracking algorithms do not yet factor in the potential leftwards migration (shortening range)~~broadening~~ of the waveform leading edge that could be caused by ~~multiple 'blurred'~~ radar responses from the snow surface and historically buried snow interfaces~~ with a vertical scale smaller than the range resolution of the sensor~~.

4.2 The Azimuth Sectoring Approach and Interdependence of Wind and Snow Properties on Backscatter

Azimuth sectoring provides an assessment of the backscatter heterogeneity across the radar scan area, here linked to the dynamic evolution of snow bedforms during wind events. Our results show how sensitive the KuKa backscatter is~~backscatter~~~~radar is~~ to development of snow bedforms and changing snow surface heights within the scan area with a directionality corresponding to prevailing wind speed and direction.

The demonstrated~~This study highlights the~~ influence of snowscape evolution from~~during~~ wind events ~~on backscatter,~~ prompt~~sing~~ the need for further investigation of the relative contributions of snow density, surface roughness and snow grain size ~~temperature gradients~~ on Ka- and Ku-b~~B~~and~~Kuband~~ backscatter. There are three main considerations: 1) ~~'radar-scale'~~ measurement and parameterization of snow surface roughness on the scale of the radar wavelength are poorly understood, especially with regard to~~its~~ temporal variability; 2) wind induces rapid density evolution at the snow surface~~of snow density~~ (Filhol & Sturm, 2015); and 3) strong covariance exists between snow~~ temperature, surface~~ density and snow temperature gradient metamorphosis and snow grain size~~roughness~~ (Colbeck, 1989). Although there is no time series of density profiles available for the RSS, we show a clear increase in density of the upper snowpack within profiles at comparable locations nearby the RSS (Figure 4). As a snow surface densifies~~becomes denser~~, surface scattering increases due to the enhanced ~~air/snow~~ dielectric contrast. Moreover, as snow warms~~becomes warmer~~, temperature-gradient driven metamorphism leads to ~~snow surface and volume~~ density changes, which can also~~in turn~~ modify the roughness of surface and/or internal interfaces, resulting in changes to backscatter (Lacroix et al., 2009).

The waveform analysis ~~does~~ provides some insights~~formation~~ on the effects of wind vs temperature. In a previous study, the significant increase in C-band backscatter after a storm was attributed to enhanced radar-scale snow surface roughness and increasing moisture content in snow with temperatures > -6°C (Komarov et al., 2017). Strong contributions from snow grain volume scattering at C-band prior to the storm were masked by dominant surface scattering after wind roughening and mechanical break-up of the snow grains during wind redistribution. In our study, the air and snow surface temperature did not reach -12°C until late on 11 November (Figures 2 and 3), but the increasing wind speeds during WE1 (Figure 2) were already switching the dominant scattering surface from being a mixture of the air/snow and snow/ice interface (prior to the wind events), to almost exclusively the air/snow interface, and increasing the backscatter associated with the air/snow interface by ~ 5 dB (Figure 8). The action of the wind on the snow surface dominated the change in the scattering surface~~, and not the increase in air and snow temperature which followed~~. Therefore, we suggest the effect of the wind on the snow roughness and/or on the snow density (wind compaction of the top layer) (Figure 4) causes the air/snow interface to increasingly become the dominant scattering surface at Ka- and Ku-band frequencies.

~~4.3 Azimuth Sectoring and Phase Difference~~

~~Azimuth sectoring provides an assessment of the backscatter heterogeneity across the radar footprint, linked to the dynamic evolution of snow bedforms produced during WE1 and WE2 (Figures 10 and 11). Our results show how sensitive the KuKa radar is to development of snow bedforms and changing snow surface heights along distinct azimuth sectors within the footprint with a directionality trend in backscatter, as a function of prevailing wind speed and direction.~~

~~Wind-induced snow deposition and snow metamorphism due to high-temperature gradients modified the Ka- and Ku-band CPD signatures as a function of snow structural anisotropy (Figure 12). This anisotropy induces scale-dependent snow thermal and dielectric properties (Leinss et al., 2016), further altering the snow surface and interface roughness regimes, and in turn modifies backscatter and CPD signatures. In general, Ka-band CPD values are higher than Ku-band. At higher frequencies, more wavelengths fall within the radar wave propagation path length through the snowpack, and the derived CPD becomes larger (Voglimacci-Stephanopoli et al., 2022; Leinss et al., 2016).~~

~~We also observed strong reversals in the CPD following WE2 (Figure 12). CPD reversals could be linked to the wind roughening of the air/snow interface during WE2, increasing the chances for multiple scattering/Fresnel reflection in shorter Ka- and Ku-band wavelengths (Ulaby et al., 1987). The observed phase shift reversals suggest the utility of Ka- and Ku-band~~

~~CPD to detect and discriminate newly deposited snow and older snow that has undergone temperature gradient metamorphism. Positive phase shifts indicate newly deposited snow (e.g. negative sectors during WE2), while negative phase shifts indicate older/metamorphosed snow (e.g. positive sectors throughout WE1 and WE2). In this study, CPD shifts due to two-way propagation through the snow are not considered because the measured range distances for VV and HH are not significantly different.~~

5. Conclusions

This study details the impact of two wind events on surface-based Ka- and Ku-band radar signatures of snow on Arctic sea ice, collected during the MOSAiC expedition in November 2019. ~~Our results represent the first-ever recording of the impact of snow redistribution on the Ka- and Ku-band radar signatures of snow on sea ice.~~ The formation of snow bedforms and erosion events in the radar scan area modified the snow surface heights, and this was recorded consistently by the radar instrument, a terrestrial laser scanner and optical~~CCTV~~ imagery.

Analysis of radar waveforms demonstrated that the air/snow and snow/sea ice interfaces are visible in both frequencies and~~,~~ all polarisations and incidence angles. During wind events, ~~we show that~~ ~~, and that~~ buried air/snow interfaces remain clearly detectable at nadir, following new snow deposition. This shows that the historical conditions under which a snow cover evolves, rather than only current conditions, affect backscatter.

We conclude that wind action and its effect on snow density and surface roughness, rather than temperature, ~~(~~which remained < -10°C during the first recorded backscatter shifts~~)~~, caused the observed change in the dominant scattering interface from a mixture of air/snow and snow/sea ice interfaces, to predominantly the air/snow interface and nadir backscatter at the air/snow interface increased by up to 5 dB. This effect would likely also be manifest in waveforms detected by satellite altimeters operating at the same frequencies, e.g., AltiKa or CryoSat-2.

Compared to pre-wind conditions, nadir backscatter across the full radar azimuth increased by up to 8 dB (Ka-band) and by up to 5 dB (Ku-band) during the wind events. This was caused by the formation of snow bedforms within the radar scan area, which increased the snow surface roughness and/or density. ~~Azimuth sectoring at~~ ~~Azimuth sectoring in 5° bins reveals the~~ ~~s~~Spatial variability in backscatter was evident across the radar scan area, and that variability~~in~~ responded~~se~~ to the formation and evolution of snow bedforms, which in turn was driven by ~~caused by~~ increasing wind speeds and changing wind direction. ~~Ka- and Ku-band co-polarized phase difference signatures demonstrate the impact of wind-redistributed snow on phase shifts and its utility to differentiate newly deposited snow from metamorphosed snow on sea ice. We link this detectability to phase shifts and their dependence on temperature gradient-driven snow metamorphism, and its effect on snow crystal structural anisotropy.~~

Overall, our results from the KuKa radar provide a process-scale understanding of how wind redistribution of~~redistribution~~~~transport of~~ snow on sea ice ~~eaffects~~ can affect its topography and physical properties, and how these changes in turn can affect the radar properties of the snow cover. Our results are relevant to both satellite ~~-~~altimetry and scatterometry through changes to radar waveforms and backscatter during, and after wind events. However, ~~-~~more investigation is needed to deduce how much wind (i.e., conditions/thresholds across space and time) is needed to impact satellite waveforms. Our~~Our~~ findings ~~however~~ cannot be applied directly to satellite instruments without considering ~~the~~ differences in footprint sizes, incidence angles, and the snow and sea ice properties sampled. However, we do provide first-hand information on the frequency, incidence angle and polarisation responses of snow on sea ice, that are ~~vitally~~ important for modelling scattered radiation over an airborne and satellite footprint.

In future field-based experiments, we will aim to combine near-coincident KuKa radar data and~~,~~ snow depth measurements (Stroeve et al., 2020), ~~and~~ terrestrial laser scanner measurements of snow surface roughness and snow density profiles to better characteris~~z~~e the effect of these variables on the radar range measurements. Forthcoming KuKa radar deployments ~~campaigns~~ on Antarctic sea ice will produce further~~can further shed valuable~~ insights into ~~complex~~ snow geophysical processes (e.g. presence of slush, melt/refreeze layers, snow-ice formation etc.) that may affect snow depth and sea ice thickness retrievals from satellite radar altimetry. In a windy Arctic and the Antarctic, these methods~~our findings~~ will facilitate improved insights towards better quantifying the impact of snow redistribution on accurate retrievals of snow/sea ice parameters from satellite radar missions such as SARAL/AltiKa, CryoSat2, Sentinel-3A, Sentinel-6, SWOT, CRISTAL, and ScatSat-1.

Code and Data availability: Data used in this manuscript was produced as part of the international Multidisciplinary drifting Observatory for the Study of the Arctic Climate (MOSAiC) with the tag MOSAiC20192020 and the Project ID: AWI PS122 00. KuKa radar data are available at http://data.bas.ac.uk/full-record.php?id=GB/NERC/BAS/PDC/01437. Meteorological data collection was funded by National Science Foundation (#OPP-1724551).

Video supplement. Time-lapse video of wind events acquired by the CCTV camera (Supplemental Video 1) and animation of radar+TLS waveforms during the wind events (Supplemental Video 2) are included in the Appendix.

Author contributions. VN processed the KuKa radar data and wrote the manuscript with input from co-authors. RW processed and analyzed the KuKa radar waveforms including NRCS calculations of interfaces, overlaid TLS data on radar waveforms and produced the radar+TLS time series animation. RM processed and plotted the DTC data. DCS processed the TLS data from the raw format and wrote code for plotting and analysis of TLS data used in this paper. AJ produced the floe map for the paper. DW and DK processed the SMP data and DW produced the SMP plot. JS, RS, TG and JL provided extensive inputs and reviews to the paper. RT, JY, TN, DJ, MH, JM, GS, SH, RR, MT, MM, MS, DW, MG, CD, IR, CP, IM, and MH provided valuable editorial comments. Many co-authors helped collect data during MOSAiC.

Competing Interests: None

Acknowledgements. This work was carried out as part of the international Multidisciplinary drifting Observatory for the Study of the Arctic Climate (MOSAiC), MOSAiC20192020 and was funded to JS in part by the Canada 150 Chair program (#G00321321), the National Science Foundation (NSF) Grant #ICER 1928230, and the Natural Environment Research Council (NERC) Grants #NE/S002510/1 (also funded RW), and #NE/L002485/1. Funding was also provided to JS by the European Space Agency (grant no. PO #5001027396). This project has received funding from the European Union's Horizon 2020 research and innovation programme (# 01003826). VN was additionally supported by Canada's Marine Environmental Observation, Prediction and Response Network (MEOPAR) postdoctoral funds. MG was supported by the DOE Atmospheric System Research Program (#DE−SC0019251, #DE−SC0021341). GS, MH, AJ and SH were supported by the the German Ministry for Education and Research (BMBF) through the MOSAiC IceSense projects (#03F0866B to GS and MH; #03F0866A to AJ and SH) and by the Deutsche Forschungsgemeinschaft (DFG) through the International Research Training Group IRTG 1904 ArcTrain (#221211316). MS and DW were supported by the European Union's Horizon 2020 research and ARICE (#730965) for MOSAiC berth fees associated with the DEARice participation; and to Swiss Polar Institute grant SnowMOSAiC (#EXF−2018−003). CD was funded through the EUMETSAT MOSAiC project (#4500019119). We thank all scientific personnel and crew members involved in the expedition of the Research Vessel Polarstern during MOSAiC in 2019-2020 (AWI_PS122_00) and Thomas Johnson (University College London) for advising on plots and animations.

References

Armitage, T. W., and Kwok, R. (2021). SWOT and the ice-covered polar oceans: An exploratory analysis. *Advances in Space Research*, *68*(2), 829-842, https://doi.org/10.1016/j.asr.2019.07.006.

Armitage, T. W., & Ridout, A. L. (2015). Arctic sea ice freeboard from AltiKa and comparison with CryoSat-2 and Operation IceBridge. Geophysical Research Letters, 42(16), 6724-6731, https://doi.org/10.1002/2015GL064823.

Akitaya, E. (1974). Studies on depth hoar. *Contributions from the Institute of Low Temperature Science*, *26*, 1-67, http://hdl.handle.net/2115/20238.

Clemens-Sewall, D., Parno, M., Perovich, D., Polashenski, C., & Raphael, I. A. (2022). FlakeOut: A geometric approach to remove wind-blown snow from terrestrial laser scans. *Cold Regions Science and Technology*, 201, 103611, https://doi.org/10.1016/j.coldregions.2022.103611

Colbeck, S. C. (1989). Snow-crystal growth with varying surface temperatures and radiation penetration. *Journal of Glaciology*, 35(119), 23-29, https://doi.org/10.3189/002214389793701536

Cox, C., Gallagher, M., Shupe, M., Persson, O., & Solomon, A. (2021). 10-meter (m) meteorological flux tower measurements (Level 1 Raw), Multidisciplinary Drifting Observatory for the Study of Arctic Climate (MOSAiC), central Arctic, October 2019 - September 2020. *Arctic Data Center*. https://doi.org/10.18739/A2VM42Z5F

~~Deems, J. S., Painter, T. H., & Finnegan, D. C. (2013). Lidar measurement of snow depth: a review. *Journal of Glaciology*, 59(215), 467-479, https://doi.org/10.3189/2013JoG12J154.~~

Doviak, R. J., & Zrnić, D (1984). Doppler Radar and Weather Observations. Academic Press, 458 pp.

Filhol, S., & Sturm, M. (2015). Snow bedforms: A review, new data, and a formation model. *Journal of Geophysical Research: Earth Surface*, 120(9), 1645-1669, https://doi.org/10.1002/2015JF003529.

Fung, A. K., & Eom, H. J. (1982). Application of a combined rough surface and volume scattering theory to sea ice and snow backscatter. *IEEE Transactions on Geoscience and Remote Sensing*, (4), 528-536, https://doi.org/10.1109/TGRS.1982.350421.

~~Fung, A. K. (1994). Microwave scattering and emission models and their applications. *Norwood, MA: Artech House*, 1994.~~

~~Glissenaar, I. A., Landy, J. C., Petty, A. A., Kurtz, N. T., & Stroeve, J. C. (2021). Impacts of snow data and processing methods on the interpretation of long-term changes in Baffin Bay early spring sea ice thickness. *The Cryosphere*, 15(10), 4909-4927, https://doi.org/10.5194/tc-15-4909-2021.~~

Fetterer, F. M., Drinkwater, M. R., Jezek, K. C., Laxon, S. W., Onstott, R. G., & Ulander, L. M. (1992). Sea ice altimetry. Washington DC *American Geophysical Union Geophysical Monograph Series*, 68, 111-135.

Guerreiro, K., Fleury, S., Zakharova, E., Rémy, F., & Kouraev, A. (2016). Potential for estimation of snow depth on Arctic sea ice from CryoSat-2 and SARAL/AltiKa missions. *Remote Sensing of Environment*, 186, 339-349, https://doi.org/10.1016/j.rse.2016.07.013.

Geldsetzer, T., Mead, J. B., Yackel, J. J., Scharien, R. K., & Howell, S. E. (2007). Surface-based polarimetric C-band scatterometer for field measurements of sea ice. *IEEE Transactions on Geoscience and Remote Sensing*, 45(11), 3405-3416, https://doi.org/10.1109/TGRS.2007.907043.

Iacozza, J., & Barber, D. G. (2010). An examination of snow redistribution over smooth land-fast sea ice. *Hydrological Processes* 24(7), 850-865, https://doi.org/10.1002/hyp.7526.

Johnson, J. B., & Schneebeli, M. (1999). Characterizing the microstructural and micromechanical properties of snow. *Cold Regions Science and Technology*, 30(1-3), 91-100, https://doi.org/10.1016/S0165-232X(99)00013-0.

Komarov, A. S., Landy, J. C., Komarov, S. A., & Barber, D. G. (2017). Evaluating scattering contributions to C-band radar backscatter from snow-covered first-year sea ice at the winter–spring transition through measurement and modeling. *IEEE Transactions on Geoscience and Remote Sensing*, *55*(10), 5702-5718, https://doi.org/10.1109/TGRS.2017.2712519.

Krumpen, T., Birrien, F., Kauker, F., Rackow, T., von Albedyll, L., Angelopoulos, M., ... & Watkins, D. (2020). The MOSAiC ice floe: sediment-laden survivor from the Siberian shelf. *The Cryosphere*, 14(7), 2173-2187, https://doi.org/10.5194/tc-14-2173-2020.

Kurtz, N. T., & Farrell, S. L. (2011). Large-scale surveys of snow depth on Arctic sea ice from Operation IceBridge. *Geophysical Research Letters*, 38(20), https://doi.org/10.1029/2011GL049216.

Kwok, R., & Cunningham, G. F. (2008). ICESat over Arctic sea ice: Estimation of snow depth and ice thickness. *Journal of Geophysical Research: Oceans*, *113*(C8), https://doi.org/10.1029/2008JC004753.

Kern, M., Cullen, R., Berruti, B., Bouffard, J., Casal, T., Drinkwater, M. R., ... & Yackel, J. (2020). The Copernicus Polar Ice and Snow Topography Altimeter (CRISTAL) high-priority candidate mission. *The Cryosphere*, *14*(7), 2235-2251, https://doi.org/10.5194/tc-14-2235-2020.

King, J., Howell, S., Brady, M., Toose, P., Derksen, C., Haas, C., & Beckers, J. (2020). Local-scale variability of snow density on Arctic sea ice. *The Cryosphere*, 14(12), 4323-4339, https://doi.org/10.5194/tc-14-4323-2020.

Löwe, H., Spiegel, J. K., & Schneebeli, M. (2011). Interfacial and structural relaxations of snow under isothermal conditions. *Journal of Glaciology*, 57(203), 499-510, https://doi.org/10.3189/002214311796905569.

Landy, J. C., Tsamados, M., & Scharien, R. K. (2019). A facet-based numerical model for simulating SAR altimeter echoes from heterogeneous sea ice surfaces. *IEEE Transactions on Geoscience and Remote Sensing*, 57(7), 4164-4180, https://doi.org/10.1109/TGRS.2018.2889763.

Leinss, S., Lemmetyinen, J., Wiesmann, A., & Hajnsek, I. (2014, June). Snow Structure Evolution Measured by Ground Based Polarimetric Phase Differences. In EUSAR 2014; 10th European Conference on Synthetic Aperture Radar (pp. 1-4). VDE.

~~Leinss, S., Löwe, H., Proksch, M., & Kontu, A. (2020). Modeling the evolution of the structural anisotropy of snow. *The Cryosphere*, 14(1), 51-75, https://doi.org/10.5194/tc-14-51-2020.~~

~~Leinss, S., Löwe, H., Proksch, M., Lemmetyinen, J., Wiesmann, A., & Hajnsek, I. (2016). Anisotropy of seasonal snow measured by polarimetric phase differences in radar time series. *The Cryosphere*, 10(4), 1771-1797, https://doi.org/10.5194/tc-10-1771-2016.~~

Löwe, H., Egli, L., Bartlett, S., Guala, M., and Manes, C. (2007), On the evolution of the snow surface during snowfall, *Geophys. Res. Lett*., 34, L21507, https://doi.org/10.1029/2007GL031637.

Lacroix, P., Legresy, B., Remy, F., Blarel, F., Picard, G., & Brucker, L. (2009). Rapid change of snow surface properties at Vostok, East Antarctica, revealed by altimetry and radiometry. *Remote Sensing of Environment*, 113(12), 2633-2641, https://doi.org/10.1016/j.rse.2009.07.019.

Lawrence, I. R., Tsamados, M. C., Stroeve, J. C., Armitage, T. W., & Ridout, A. L. (2018). Estimating snow depth over Arctic sea ice from calibrated dual-frequency radar freeboards. *The Cryosphere*, 12(11), 3551-3564, https://doi.org/10.5194/tc-12-3551-2018.

Lawrence, I. R., Armitage, T. W., Tsamados, M. C., Stroeve, J. C., Dinardo, S., Ridout, A. L., ... & Shepherd, A. (2021). Extending the Arctic sea ice freeboard and sea level record with the Sentinel-3 radar altimeters. Advances in Space Research, 68(2), 711-723, https://doi.org/10.1016/j.asr.2019.10.011.

Moon, W., Nandan, V., Scharien, R. K., Wilkinson, J., Yackel, J. J., Barrett, A., ... & Else, B. (2019). Physical length scales of wind-blown snow redistribution and accumulation on relatively smooth Arctic first-year sea ice. *Environmental Research Letters*, 14(10), 104003, https://doi.org/10.1088/1748-9326/ab3b8d

Nab, C., Mallett, R., Gregory, W., Landy, J., Lawrence, I., Willatt, R., ... & Tsamados, M. (2023). Synoptic variability in satellite altimeter-derived radar freeboard of Arctic sea ice. Geophysical Research Letters, e2022GL100696, https://doi.org/10.1029/2022GL100696

Nandan, V., Scharien, R., Geldsetzer, T., Mahmud, M., Yackel, J. J., Islam, T., ... & Duguay, C. (2017). Geophysical and atmospheric controls on Ku-, X-and C-band backscatter evolution from a saline snow cover on first-year sea ice from late-winter to pre-early melt. Remote Sensing of Environment, 198, 425-441, https://doi.org/10.1016/j.rse.2017.06.029

Nicolaus, M., Perovich, D. K., Spreen, G., Granskog, M. A., von Albedyll, L., Angelopoulos, M., ... & Wendisch, M. (2022). Overview of the MOSAiC expedition: Snow and sea ice. *Elem Sci Anth*, 10(1), 000046, https://doi.org/10.1525/elementa.2021.000046.

Proksch, M., Löwe, H., & Schneebeli, M. (2015). Density, specific surface area, and correlation length of snow measured by high-resolution penetrometry. *Journal of Geophysical Research: Earth Surface*, 120(2), 346-362, https://doi.org/10.1002/2014JF003266.

Segal, R. A., Scharien, R. K., Cafarella, S., & Tedstone, A. (2020). Characterizing winter landfast sea-ice surface roughness in the Canadian Arctic Archipelago using Sentinel-1 synthetic aperture radar and the Multi-angle Imaging SpectroRadiometer. *Annals of Glaciology*, 61(83), 284-298, https://doi.org/10.1017/aog.2020.48.

Sturm, M., K. Morris, and R. Massom (1998), The winter snow cover of the West Antarctic pack ice: Its spatial and temporal variability, *in Antarctic Sea Ice: Physical Processes, Interactions and Variability*, *Antarct. Res. Ser.*, vol. 74, edited by M. O. Jeffries, pp. 1–18, AGU, Washington, D. C, https://doi.org/10.1029/AR074p0001.

Savelyev, S. A., Gordon, M., Hanesiak, J., Papakyriakou, T., & Taylor, P. A. (2006). Blowing snow studies in the Canadian Arctic shelf exchange study, 2003–04. *Hydrological Processes*, *20*(4), 817-827, https://doi.org/10.1002/hyp.6118.

Stroeve, J., Nandan, V., Willatt, R., Tonboe, R., Hendricks, S., Ricker, R., ... & Tsamados, M. (2020). Surface-based Ku-and Ka-band polarimetric radar for sea ice studies. *The Cryosphere*, 14(12), 4405-4426, https://doi.org/10.5194/tc-14-4405-2020.

~~Stroeve, J., Nandan, V., Willatt, R., Dadic, R., Rotosky, P., Gallagher, M., ... & Schneebeli, M. (2022). Rain-on-Snow (ROS) Understudied in Sea Ice Remote Sensing: A Multi-Sensor Analysis of ROS during MOSAiC. *The Cryosphere Discussions*, 1-42, https://doi.org/10.5194/tc-2021-383.~~

Singh, U. S., & Singh, R. K. (2020). Application of maximum-likelihood classification for segregation between Arctic multi-year ice and first-year ice using SCATSAT-1 data. *Remote Sensing Applications: Society and Environment*, 100310, https://doi.org/10.1016/j.rsase.2020.100310.

Spreen, Gunnar; Huntemann, Marcus; Thielke, Linda; Naderpour, Reza; Mahmud, Mallik; Tavri, Aikaterini (2022): Infrared camera raw data (ir_variocam_01) at the remote sensing site on the ice floe during MOSAiC expedition 2019/2020. *PANGAEA*, https://doi.org/10.1594/PANGAEA.940717

Spreen, Gunnar; Huntemann, Marcus; Naderpour, Reza; Mahmud, Mallik; Tavri, Aikaterini; Thielke, Linda (2021): Optical IP Camera images (VIS_INFRALAN_01) at the remote sensing site on the ice floe during MOSAiC expedition 2019/2020. *PANGAEA*, https://doi.org/10.1594/PANGAEA.939362

Trujillo, E., Leonard, K., Maksym, T., and Lehning, M. (2016), Changes in snow distribution and surface topography following a snowstorm on Antarctic sea ice, *J. Geophys. Res. Earth Surf.*, 121, 2172– 2191, https://doi.org/10.1002/2016JF003893.

Tilling, R. L., Ridout, A., & Shepherd, A. (2018). Estimating Arctic sea ice thickness and volume using CryoSat-2 radar altimeter data. *Advances in Space Research*, *62*(6), 1203-1225, https://doi.org/10.1016/j.asr.2017.10.051.

Ulaby, F. T., Held, D., Dodson, M. C., McDonald, K. C., & Senior, T. B. (1987). Relating polarization phase difference of SAR signals to scene properties. *IEEE Transactions on Geoscience and Remote Sensing*, (1), 83-92, https://doi.org/10.1109/TGRS.1987.289784.

Ulaby, F. T., Long, D. G., Blackwell, W. J., Elachi, C., Fung, A. K., Ruf, C., ... & Van Zyl, J. (2014). *Microwave radar and radiometric remote sensing* (Vol. 4, No. 5, p. 6). Ann Arbor, MI, USA: University of Michigan Press.

Virtanen, P., Gommers, R., Oliphant, T. E., Haberland, M., Reddy, T., Cournapeau, D., ... & Van Mulbregt, P. (2020). SciPy 1.0: fundamental algorithms for scientific computing in Python. *Nature methods*, *17*(3), 261-272, https://doi.org/10.1038/s41592-019-0686-2.

~~Voglimacci-Stephanopoli, J., Wendleder, A., Lantuit, H., Langlois, A., Stettner, S., Schmitt, A., Dedieu, J-P., Roth, A., & Royer, A (2022). Potential of X-band polarimetric synthetic aperture radar co-polar phase difference for arctic snow depth estimation, *The Cryosphere*, 16, 2163–2181, https://doi.org/10.5194/tc-16-2163-2022.~~

Willatt, R. C., Giles, K. A., Laxon, S. W., Stone-Drake, L., & Worby, A. P. (2009). Field investigations of Ku-band radar penetration into snow cover on Antarctic sea ice. *IEEE Transactions on Geoscience and remote sensing*, *48*(1), 365-372, https://doi.org/10.1109/TGRS.2009.2028237.

Wingham, D. J., Francis, C. R., Baker, S., Bouzinac, C., Brockley, D., Cullen, R., ... & Wallis, D. W. (2006). CryoSat: A mission to determine the fluctuations in Earth's land and marine ice fields. *Advances in Space Research*, 37(4), 841-871, https://doi.org/10.1016/j.asr.2005.07.027.

Wagner, D. N., Shupe, M. D., Cox, C., Persson, O. G., Uttal, T., Frey, M. M., ... & Lehning, M. (2022). Snowfall and snow accumulation during the MOSAiC winter and spring seasons. The Cryosphere, 16(6), 2373-2402, https://doi.org/10.5194/tc-16-2373-2022.

Yackel, J. J., & Barber, D. G. (2007). Observations of snow water equivalent change on landfast first-year sea ice in winter using synthetic aperture radar data. *IEEE Transactions on Geoscience and Remote Sensing*, 45(4), 1005-1015, https://doi.org/10.1109/TGRS.2006.890418.